DETERMINATION OF SNOW WATER EQUIVALENT USING GROUND-PENETRATING RADAR FROM AN AERIAL PLATFORM

by

Jonah A. G. Bartrand

A thesis submitted to the Faculty and the Board of Trustees of the Colorado School of Mines in partial fulfillment of the requirements for the degree of Master of Science (Geophysics).

Golden, Colorado

Date ____________________

Signed: ____________________
Jonah A. G. Bartrand

Signed: ____________________
Dr. John Bradford
Thesis Advisor

Golden, Colorado

Date ____________________

Signed: ____________________
Dr. Paul Sava
Professor and Head
Department of Geophysics

ABSTRACT

Alpine snowpack accounts for a majority of summer surface stream flow in many areas of the western US. This surface water supports, agriculture, municipal water supplies, recreation, and fisheries. Annual variations in total snowpack complicate efficient allocation of this important, finite resource. To improve the accuracy and ease of snow water equivalent (SWE) surveys, we propose using of ground-penetrating radar (GPR) from a low-flying aerial platform to quantify SWE quickly and accurately in both wet and dry snow. We present a method for producing synthetic data and a workflow for recovering SWE from noisy data by combining velocities derived from diffraction analysis and Q^* derived from spectral peak comparisons. Our recovered SWE values have an average error of 11.0% in wet and dry snow. Aerial GPR has the potential to effectively quantify snowpack SWE, providing a valuable tool for water managers to improve the quality of life for those that rely on this important resource.

TABLE OF CONTENTS

LIST OF FIGURES AND TABLES

LIST OF SYMBOLS

permeability, free space	μ_0
permittivity, free space	ε_0
permittivity, complex	ϵ^*
permittivity, real	ε'
permittivity, imaginary	ε”
permittivity, static	ϵ_s
permittivity, optical	ϵ_∞
conductivity	σ
porosity	ϕ
density	rho
volumetric water content	W
D-field relaxation time	τ_D
E-field relaxation time	τ_E
electric field	E
magnetic field	H
memory variable	m
wave number, complex	k^*
wave number, real	k'
wave number, imaginary	k”
reflectivity	R

source wavelet . . . S

velocity, interval . . . v_{int}

error, interval velocity . . . δ_{int}

velocity, root mean square . . . v_{rms}

error, rms velocity . . . δ_{rms}

frequency . . . f

error, frequency . . . δ_f

frequency, angular . . . ω

quality factor, frequency-dependent . . . Q^*

error, Q^* . . . δ_{Q^*}

error, real permittivity . . . $\delta_{\varepsilon'}$

error, imaginary permittivity . . . $\delta_{\varepsilon''}$

error, density . . . δ_{rho}

error, volumetric water content . . . δ_W

depth . . . z

time . . . t

ACKNOWLEDGMENTS

After the years of research necessary to arrive at this point, where acknowledgments will be formally recorded for posterity, it is with a great sense of relief that I memorialize those individuals most responsible for my completion of this thesis.

My parents are responsible for supporting me physically, financially, and developmentally for the last 25 years. Though they were not directly involved in my research, nor in the writing and editing of this thesis, they have been instrumental in providing a sense of security and inspiration which led to its completion.

Eight years ago, Danny Perea, a scientist of the highest caliber, provided a high school student with a job and an entrance into the world of scientific research. Though the content of this thesis bears little relation to Atom-Probe Tomography, Danny gave me the inspiration to pursue research as an undergraduate and the opportunity to explore the impact that programming can have on scientific research. His initial encouragement to learn how to leverage the power of automation was the beginning of my love-hate relationship with programming.

At the University of Idaho, I worked with several professors as research assistants. Dave McIlroy gave me a project two weeks into my freshman year. Two years later, I learned that not all research projects are successful. Linh Nguyen gave me a job modeling acoustic wave propagation, an experience directly relevant to the forward modeling section of this thesis. He also showed me that research can lead in unexpected directions. There are connections between seemingly unrelated fields that can be fascinating to explore. To Rob Abbott and the IRIS program, I owe thanks for providing me with an introduction to geophysics.

The single individual most responsible for the completion of this thesis - aside from the author - is John Bradford, my advising professor. John offered me a position in a field with which I had little experience. He found the time to work with me, in spite of his other obligations, as this project morphed from fieldwork to numerical modeling over the course of three years. His continued support was indispensable in the completion of this work. Jeff Shragge and Paul Sava, my other committee members, provided valuable advice and recommendations throughout the process. And when I encountered a problem with Mio, Jeff solved the issue in a matter of minutes.

There are many other individuals to which I am indebted: those mentioned above are most responsible for my decision to pursue and complete a Master's degree. However, I would be remiss if I did not acknowledge the individual who made the greatest sacrifice so that I could be where I am today. Two thousand years ago, the God responsible for my creation offered up His own life in exchange for my own. Without Him, this world would be a much darker place.

CHAPTER 1
INTRODUCTION

1.1 Importance of Mountain Snowpack

In the year 2000, more than one sixth of the global population lived in areas where snow melt supplies more than half of the total surface water discharge [1]. In the United States, the states west of the Mississippi River are especially dependent on snowpack, with 53% of total runoff originating as snow, and 70% in mountainous regions [2]. This runoff impacts all aspects of life for individuals in these areas, from municipal water supplies and agricultural irrigation to aquatic recreation and native ecosystems. Water managers at the state and local levels have to determine how to allocate this water to satisfy these competing interests.

However, the yearly snowpack levels can vary wildly from year to year. From 1968 to 2019, the state of Colorado saw April 1 snowpack range from 148% to 48% of the average [3]. With such variability, foreknowledge of the total amount of water stored in mountain snowpack is critical to ensuring that all available water is properly utilized. This task takes on more importance when we consider snowmelt that crosses state lines. For example, the Colorado River Compact governs the distribution to the signatory states of all water in the Colorado River Basin. However, equitable allocation of this water requires an accurate knowledge of how much water will be available in the water year. Water managers would benefit from snow survey methods that can accurately predict the total discharge in a basin that will result from snow melt.

1.2 Current Snowpack Measurement Techniques

Currently, snowpack monitoring in the United States relies on SNOTEL stations, permanently emplaced stations that provide real-time snow information. These stations measure snow water equivalent (SWE) using a large, oil-filled pillow with an attached pressure gauge. As snow accumulates on the pillow, the hydrostatic pressure in the pillow increases. The pressure increase provides a direct measure of the weight of overlying snow per unit area. The SNOTEL network includes more than 800 stations in mountainous areas of 13 western states [4]. Some stations have been in place since the 1960s, providing an accurate measure of historical snowpack trends. However, these stations are very sparsely distributed. The Central Rockies region covers approximately 400,000 km^2 from northern New Mexico to southern Montana, including the headwaters of the Rio Grande, Platte, Arkansas, Snake, and Colorado Rivers. Within this region there are 240 SNOTEL stations, yielding a station density of one station per 1700 km^2. Interpolation of sparsely distributed SNOTEL data to continuous, basin-scale snow depth maps requires additional topographical information about the SNOTEL site and basin, and are still plagued by errors arising from the sparsity of data points [5]. Water management agencies also use snowcourses and snowpits, which record snow depth and density with depth. However, such direct sampling methods are time-intensive, with a single snowpit potentially requiring several man-hours to excavate and sample. Consequently, these methods are primarily used for calibrating and validating SNOTEL data. Correlation of SNOTEL data with stream gauges is the primary method for forecasting water availability, but a changing climate means that historical trends will not necessarily be accurate predictors for the future. A technique that can remotely sense SWE and rapidly cover large areas is necessary to improve SWE prediction.

1.3 Snow Remote Sensing Methods

Numerous remote sensing techniques with the potential for rapid mapping of snow coverage and depth have recently emerged. Ideally, SWE maps would be generated in near-real time from satellite data. Visible-wavelength (LandSat) and thermal (MODIS) imagers are used to map areal snow coverage, but cannot produce information on snow depth or density. Other techniques use passive microwave imaging to produce snow maps, but are subject to large errors due to source variability, topography, vegetation cover, and other factors [6].

The most promising techniques to date utilize LIDAR and visible-wavelength imaging from aerial platforms for basin-scale mapping of surface elevation changes. As a baseline digital elevation model, a survey when no snow is on the ground is conducted in late summer. Subsequent surveys with snow on the ground yield new digital elevation models. Presumably, any variation between the two is due to snow accumulations, so a snow depth model can be produced by subtracting the baseline. This technique can quickly map very large areas and produce snow depth maps in near-real time. However, snow density and liquid water content must be assumed or determined from other techniques [7].

1.4 Ground-Penetrating Radar

Ground-penetrating radar is an active-source, electromagnetic geophysical technique that is sensitive to permittivity and conductivity contrasts in the subsurface. In a pulsed GPR system, a wavelet pulse with a fixed center frequency is emitted by a transmitting antenna and the returned signal is received on a receiver antenna. The wavelet center frequency can range from 10 MHz to 10 GHz, with a higher frequency providing better resolution, but a smaller depth of penetration. The depth of investigation of GPR is affected by the material conductivity and permittivity (Table 1.1) and the radar center frequency.

Table 1.1: Typical relative permittivity, electrical conductivity, velocity, and attenuation observed in common geologic materials [8].

Material	ε'	σ (mS/m)	v (m/ns)	α (dB/m)
Air	1	0	0.3	0
Distilled water	80	0.001	0.033	2×10^{-3}
Fresh water	80	0.5	0.033	0.1
Sea water	80	3000	0.01	103
Dry sand	3-5	0.01	0.15	0.01
Saturated sand	20-30	1-10	0.06	0.03-0.3
Limestone	4-8	0.5-2	0.12	0.4-1
Shales	5-15	1-100	0.09	1-100
Silts	5-30	1-100	0.07	1-100
Clays	5-40	2-1000	0.06	1-300
Granite	4-6	0.01-1	0.13	0.01-1
Dry salt	5-6	0.01-1	0.13	0.01-1
Ice	3-4	0.01	0.16	0.01

To establish SWE along a particular transect, one must determine depth, density, and liquid water content. Using GPR data alone, calculating the snow depth requires the low-conductivity radar velocity approximation:

$$v \approx \frac{1}{\sqrt{\varepsilon' \mu}}, \tag{1.1}$$

where ε' is the real permittivity of the material and μ is the permeability of the material - assumed to equal $\mu_0 \approx 1.257 \times 10^{-6}$ kg/(s^{2}A^2) for most geologic materials including snow.

Snow is a composite material consisting of air, ice, and liquid water if partial melt has occurred. When snow temperatures are below freezing, there is no liquid water present and the snow density can be determined from empirical relationships between snow density and radar velocity [9]. Figure 1.1 shows how the radar velocity in snow varies with both dry snow density ρ_d and volumetric water content W. The velocity of radar in snow can be determined by a number of methods, depending on the survey methods utilized. For an aerial survey, fixed-offset data are the easiest to collect. With this type of data, diffraction analysis is a straightforward method to determine radar velocity.

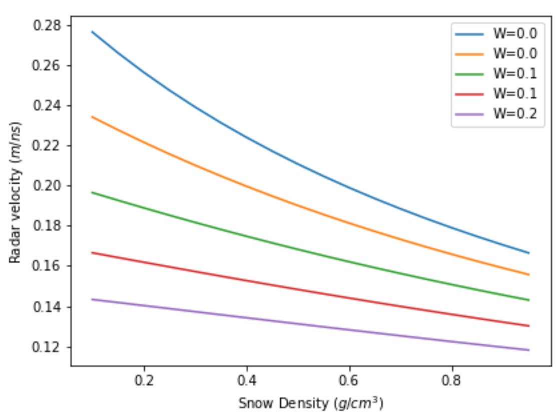

Figure 1.1: Radar velocity in snow as function of dry snow density ρ_d and water saturation W. When snow is dry, the radar velocity is strictly a function of the snow density. With liquid water present, the radar velocity depends much more on the water saturation, but snow density still has an impact.

Several authors have shown accurate recovery of SWE from GPR surveys assuming dry snow [10–21]. Early in the snow accumulation season, assuming dry snow is reasonable. But at the time of peak SWE, some melting of the snow has already occurred (W>0). Dry snow analysis methods are unable to accurately quantify SWE at peak snowpack. When liquid water is present in the snow, the radar velocity depends upon both the snow density and the fraction of liquid water present [9]. Some overcome this limitation by combining GPR with snow depth sensors [22, 23]. However, Bradford et al. [24] show that W can be determined with GPR data alone.

The attenuation characteristics of a radar pulse depend on the propagation medium. Different media have different relaxation frequencies which govern the amount of frequency-dependent attenuation of a radar pulse. Ice has a relaxation frequency lower than the typical frequency range for GPR, so we approximate the permittivity of ice as frequency-independent. Liquid water has a relaxation frequency sufficiently close to GPR frequencies to cause significant frequency-dependent attenuation. When snow is dry, there is no frequency-dependent attenuation of the reflected radar pulse due to intrinsic material properties. However, when snow is wet, the liquid water causes the higher frequency components of the pulse to attenuate more quickly than lower frequency components. By quantifying the strength of the frequency-dependent attenuation of the reflected pulse, W of the snow can be estimated. With an estimate of W and the radar velocity in the snow, the dry snow density can be determined from empirical relationships, like those given by Tiuri et al. [9].

We implement a two-dimensional forward model that incorporates Debye permittivity relaxation [25]. Synthetic zero-offset radar data are then generated assuming homogeneus and heterogeneous, dry and wet snow. We then develop a largely automated algorithm to determine snow radar velocity by diffraction analysis and liquid water content from frequency-dependent attenuation characteristics. This approach allows for the use of aerial GPR data to quickly estimate SWE in both wet and dry snow with no ground measurements necessary. This development will lead to improved safety, speed, and accuracy for snow surveys.

CHAPTER 2

METHODOLOGY

2.1 Data Simulation

2.1.1 Forward Modeling with Attenuation

To accurately model the frequency-dependent attenuation that occurs in wet snow, we utilized a FDTD, two-dimensional wave solver (equations 2.1-2.4) developed by Bergmann et al. [25]. The wave solver utilizes coupled, first-order partial differential equations to propagate the transverse electric field E_y and coupled magnetic fields H_x and H_z forward in time,

$$\varepsilon_\infty^e \frac{\partial E_y}{\partial t} = \frac{\partial H_x}{\partial z} - \frac{\partial H_z}{\partial x} - \sigma_\infty^e E_y - \varepsilon_s \sum_{\ell=1}^{L} m_\ell \tag{2.1}$$

$$\frac{\partial m_\ell}{\partial t} = -\frac{1}{\tau_{D\ell}} m_\ell - \frac{1}{L}\left[\sum_{\ell=1}^{L} \frac{1}{\tau_{D\ell}^2}\left(1 - \frac{\tau_{E\ell}}{\tau_{D\ell}}\right)\right] E_y, 1 \leq \ell \leq L \tag{2.2}$$

$$\mu \frac{\partial H_x}{\partial t} = \frac{\partial E_y}{\partial z} \tag{2.3}$$

$$-\mu \frac{\partial H_z}{\partial t} = \frac{\partial E_y}{\partial x} \tag{2.4}$$

where ε_s is the static permittivity and ε_∞^e and σ_∞^e are the effective optical permittivity and conductivity, respectively. To account for the attenuation caused by L Debye peaks, each characterized by a pair of relaxation times $\tau_{D\ell}$ and $\tau_{E\ell}$, L memory variables $m_\ell, 1 \leq \ell \leq L$ are introduced. The two relaxation parameters, τ_{El} and τ_{Dl}, are the $\boldsymbol{E}-$ and $\boldsymbol{D}-$ field relaxation times, respectively [25]. The time-dependent relaxation of the medium permittivity from ε_∞^e to ε_s with a characteristic relaxation time τ_D is

$$\varepsilon(t) = \varepsilon_s \left[1 - \frac{1}{L}\sum_{\ell=1}^{L}\left(1 - \frac{\tau_{E\ell}}{\tau_{D\ell}}\right) e^{-t/\tau_{D\ell}}\right] \mathcal{H}(t), \tag{2.5}$$

where $\mathcal{H}(t)$ is the Heaviside Function. At $t = 0$

$$\varepsilon(0) = \varepsilon_\infty \frac{\varepsilon_s}{L} \sum_{\ell=1}^{L} \frac{\tau_{E\ell}}{\tau_{D\ell}}, \tag{2.6}$$

and as $t \to \infty$

$$\varepsilon(t \to \infty) = \varepsilon_s. \tag{2.7}$$

To create a model with L Debye peaks, a total of $L + 3$ total equations are required. For modeling snow, only one Debye peak ($L = 1$) is needed to account for relaxation of liquid water.

The discretized form of equations 2.1-2.4 utilizes a temporally and spatially staggered grid:

$$H_{x_{x+1/2,z+1/2}}^{n+1/2} = H_{x_{x+1/2,z+1/2}}^{n-1/2} + \frac{\Delta t}{\mu} \frac{-E_{y_{x,z+2}}^{n} + 27E_{y_{x,z+1}}^{n} - 27E_{y_{x,z}}^{n} + E_{y_{x,z-1}}^{n}}{24\Delta z} \tag{2.8}$$

$$H_{z_{x+1/2,z+1/2}}^{n+1/2} = H_{z_{x+1/2,z+1/2}}^{n-1/2} - \frac{\Delta t}{\mu} \frac{-E_{y_{x+2,z}}^{n} + 27E_{y_{x+1,z}}^{n} - 27E_{y_{x,z}}^{n} + E_{y_{x-1,z}}^{n}}{24\Delta z} \tag{2.9}$$

$$m_{x,z}^{n+1/2} = m_{x,z}^{n-1/2} - \Delta t\left[\frac{m_{x,z}^{n+1/2} + m_{x,z}^{n-1/2}}{2\tau_D} + \frac{1}{\tau_D^2}\left(1 - \frac{\tau_E}{\tau_D}\right)\right] E_{y_{x,z}}^{n} \tag{2.10}$$

$$\begin{aligned} E_{y_{x,z}}^{n+1} = E_{y_{x,z}}^{n} + \frac{\Delta t}{\varepsilon_\infty^e}\Big[& \frac{-H_{x_{x,z+3/2}}^{n+1/2} + 27H_{x_{x,z+1/2}}^{n+1/2} - 27H_{x_{x,z-1/2}}^{n+1/2} + H_{x_{x,z-3/2}}^{n+1/2}}{24\Delta z} \\ & - \frac{-H_{z_{x+3/2,z}}^{n+1/2} + 27H_{z_{x+1/2,z}}^{n+1/2} - 27H_{z_{x-1/2,z}}^{n+1/2} + H_{z_{x-3/2,z}}^{n+1/2}}{24\Delta x} \\ & - \sigma_\infty^e\left(E_{y_{x,z}}^{n+1} + E_{y_{x,z}}^{n}\right) - \varepsilon_s m_{x,z}^{n+1/2}\Big] \end{aligned}, \tag{2.11}$$

where $H_{x_{i,j}}^{n+1/2}$ is the value of the $(n + 1/2)^{th}$ time step of H_x at the i^{th} row and j^{th} column. The same index notation is applied to H_z, m, and E_y. Δt, Δx, and Δz are the discretization steps for t, x, an z, respectively. Per the numerical analysis of Bergmann et al., a second-order finite-difference approximation of the spatial derivatives offers the best compromise between computational efficiency and minimization of numerical dispersion [25].

2.1.2 Conductivity

The material properties for each layer within the snow are calculated using the dry snow density, ρ_d, and the snow saturation, W. Archie's Law is an empirically derived formula to predict the conductivity of a uniform sand-water mixture [26]

$$\sigma_{mixture} = \frac{1}{a}\sigma_w \phi^m W^n, \tag{2.12}$$

where $\sigma_{mixture}$ is the conductivity of the mixture, σ_w is the conductivity of the pore fluid (water), ϕ is the porosity of the sand matrix, W is the volumetric fluid content, or saturation, of the matrix, and a, m and n are empirically determined coefficients. Archie's Law assumes that the conductivity of the matrix material is negligible relative to the conductivity of the pore fluid. For snow, this is an appropriate assumption, since the conductivity of dry snow crystals (ice) is $\sigma_i = 0.01$ mS/m, while the conductivity of fresh water is $\sigma_w = 0.5$ mS/m (Table 1.1). Therefore, we assume the conductivity of ice is negligible, relative to that of snow melt. The ϕ of snow can be calculated from ρ_d by

$$\phi_{snow} = 1 - \frac{\rho_d}{\rho_{ice}}, \tag{2.13}$$

where the density of ice $\rho_{ice} = 0.9168\ \frac{g}{cm^3}$. The wet snow conductivity is calculated using Archie's Law (with $a = 1$, $m = 1.5$, $n = 2$):

$$\sigma_{snow} = \phi_{snow}^{1.5} W^2 \sigma_w. \tag{2.14}$$

2.1.3 Permittivity

The Complex Refractive Index Model (CRIM) provides a mixing formula to calculate the permittivity of a mixture of air, ice, and liquid water [27]. Though a general mixing model, the CRIM equation provides reasonable agreement with empirically derived petrophysical relationships specifically for snow [9]. This model calculates the complex permittivity of a mixture based on the complex permittivity ε_i^* and fraction volume θ_i of each constitutive material in the mixture,

$$\sqrt{\varepsilon^*} = \sum_i \sqrt{\varepsilon_i^*}\theta_i. \tag{2.15}$$

For snow, the constituent materials are air, ice, and water, so the mixing formula can be written:

$$\sqrt{\varepsilon^*} = \sqrt{\varepsilon_{air}^*}\theta_{air} + \sqrt{\varepsilon_{ice}^*}\theta_{ice} + \sqrt{\varepsilon_{water}^*}\theta_{water} \tag{2.16}$$

$$\sqrt{\varepsilon' + \varepsilon"i} = \theta_{air} + \sqrt{\varepsilon_{ice}^*}\theta_{ice} + \sqrt{\varepsilon_{water}^*}W \tag{2.17}$$

$$\theta_{ice} = \frac{\rho_d}{\rho_{ice}} \tag{2.18}$$

$$\theta_{air} = 1 - \theta_{ice} - W, \tag{2.19}$$

where ρ_d is the density of dry snow (in g/cm^3), $\rho_{ice} = 0.9168$ g/cm^3 is the density of ice, $\varepsilon_{ice}^* = 3.2$, ε_{water}^* is the complex permittivity of water, W is the volumetric liquid water content, and $\varepsilon' + i\varepsilon''$ is the complex permittivity of snow. Because equations 2.8-2.11 are parameterized in terms of ε_s and ε_∞, we must convert the complex permittivity of our snow mixture to ε_s and ε_∞. ε^* of water is calculated over a frequency range from $10^4 Hz \leq \omega \leq 10^{20} Hz$ using the Debye Equation (equation 2.20) [28].

$$\varepsilon^* = \frac{\varepsilon_s - \varepsilon_\infty}{1 - (i\omega\tau_D)} + \varepsilon_\infty. \tag{2.20}$$

For liquid water at $0°C$, $\varepsilon_s = 87.74\varepsilon_0$, $\varepsilon_\infty = 4.46\varepsilon_0$, and $\tau_D = 1.79 \times 10^{-11}$ s [28]. These frequency-dependent permittivity values are then used in Equation 2.15 to provide a frequency-dependent complex permittivity of the snow mixture. At low and high frequencies, the imaginary component of the complex permittivity approaches zero. The low-frequency real permittivity corresponds to ϵ_s and the high-frequency real permittivity corresponds to ϵ_∞.

2.1.4 Relaxation Times

Because liquid water is the only material in snow that has a relaxation frequency in the range of GPR frequencies, we set $\tau_D = 1.79 \times 10^{-11}$ s [28]. To determine the value of τ_E for a medium, we use the values of ε_s and ε_∞. The relationship between relaxation times and static and optical permittivities is [25]

$$\tau_E = \tau_D \frac{\epsilon_\infty}{\epsilon_s}. \tag{2.21}$$

After finding ϵ_s and ϵ_∞ for a mixture using the Cole-Cole diagram, τ_E can then be calculated to completely characterize the material properties. When $\tau_E = \tau_D$, equations 2.8-2.11 reduce to the acoustic wave equation with bulk attenuation. Consequently, τ_E governs the extent of frequency-dependent attenuation.

2.2 Data Processing

The modeling steps described above produce synthetic radargrams from media with known SWE values. However, we need to develop a process for extracting SWE from radargrams with no other information. We follow the procedure outlined by Bradford et al. [24], using diffraction analysis to recover radar velocities and spectral peak shifts to quantify the frequency-dependent attenuation.

2.2.1 Diffraction Analysis

When a sharp point or material discontinuity occurs in a medium, that location acts as a point scatterer that produces a diffraction hyperbola in common-offset GPR gathers. The depth of the scatterer z can be mapped into the time domain by assuming a constant velocity of the overlying material v. The two-way travel time of the radar pulse directly over the scatterer is $t_0 = \frac{2z}{v}$. The equation for the two-way travel time t at any horizontal offset x from the scatterer is then

$$t(x) = \sqrt{t_0^2 + \frac{4x^2}{v^2}}. \tag{2.22}$$

Figure 2.1 shows how the shape of the diffraction hyperbola changes with t_0 and v.

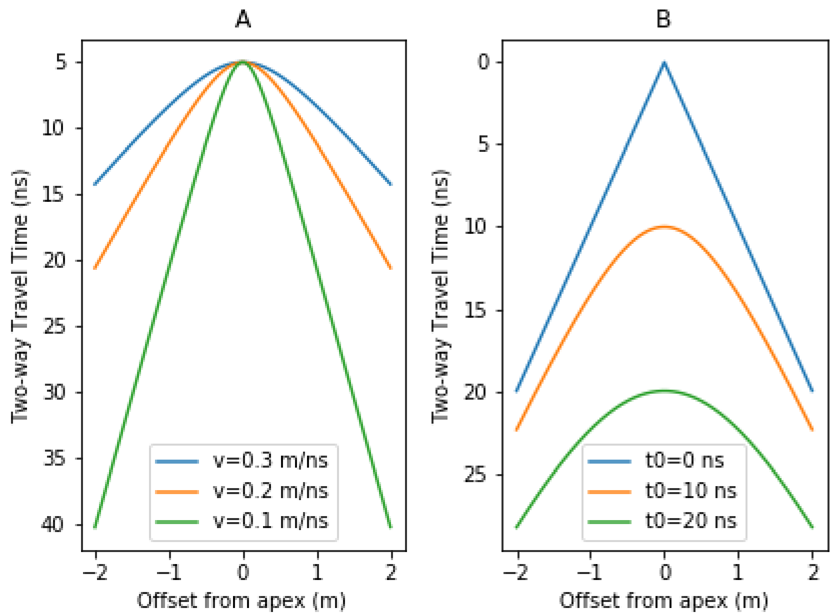

Figure 2.1: (A) Modeled diffractions at t_0 =5 ns for different overburden velocities. As the velocity decreases, the slope of the diffraction "wings" increases. (B) Modeled diffractions for v =0.2 m/ns at various depths.

With field data, the diffraction image is known and the goal is to calculate the velocity of the diffraction. We utilize an approach developed by Fomel et al. [29] and applied successfully to snow GPR surveys by St Clair and Holbrook [18]. First, specular reflections are removed to emphasize the diffractions. To accomplish this, we apply a local background subtraction that subtracts a horizontal moving average of a fixed width from the data at the center of the window. This approach is simple to implement and effectively removes all but the steepest plane reflections from the data.

Once the specular reflections in the radargram are minimized, the data are migrated with the Stolt algorithm [30] over a range of velocities. Ideally, migration will cause all diffraction energy to focus at diffraction apexes (Figure 2.2C). When migrated at a higher or lower velocity than the true RMS velocity, diffractions do not focus at the apex. To quantitatively assess the migration velocity that best focuses diffractions, the varimax norm curve of the region around each diffraction apex is calculated [29]

$$V = \frac{\sum_i s_i^4}{(\sum_i s_i^2)^2}, \tag{2.23}$$

where s_i is the amplitude of the i^{th} data point, the summations occur over the time and spatial axes of the migrated data, and V is the value of the varimax norm. Figure 2.2 shows a varimax norm curve, optimal migration, and undermigration for a pure diffraction with no noise. The velocity at which the varimax norm is maximized is the optimal migration velocity and corresponds to the RMS velocity of the diffraction. The standard error δ_{rms} of the RMS velocity estimate is calculated by assuming the peak of the varimax norm curve is Gaussian. The full width (d) of a Gaussian distribution at half the maximum height is related to the standard deviation (δ) of the distribution by

$$\delta_{rms} = d/(2\sqrt{2ln(2)}) \approx 0.424d. \tag{2.24}$$

The greater the width of the peak, the greater the uncertainty of the velocity estimate.

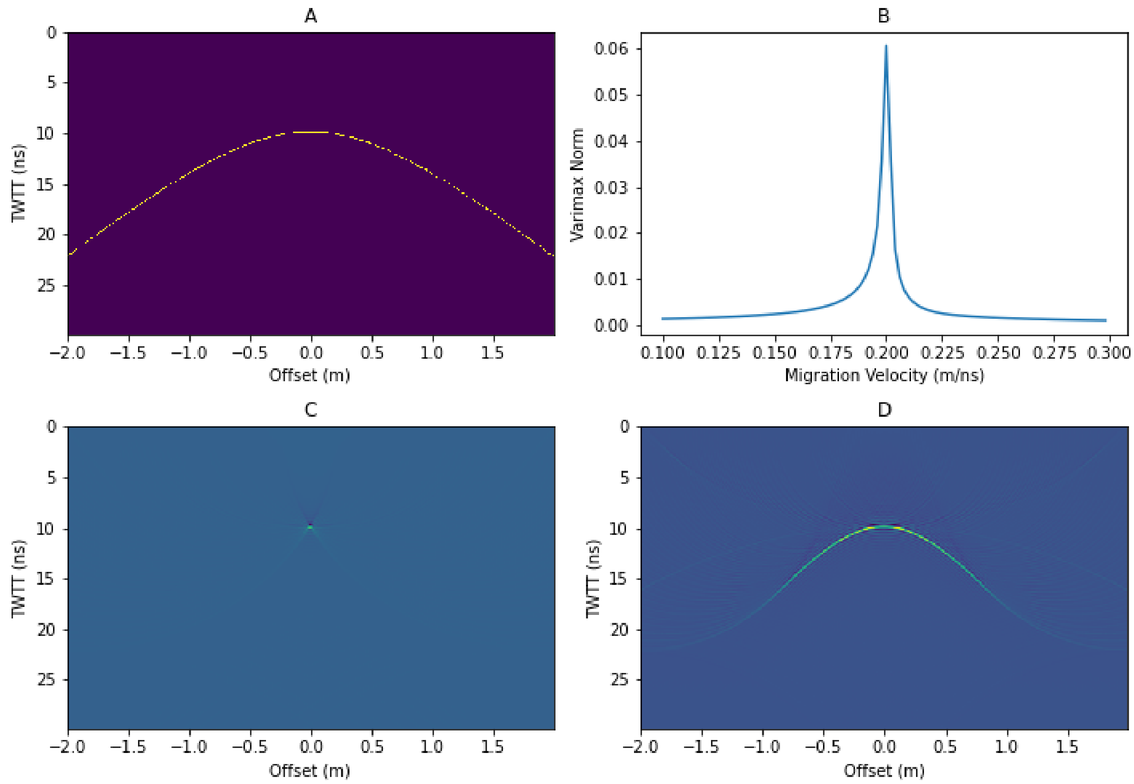

Figure 2.2: (A) Diffraction with moveout velocity of 0.2 m/ns. (B) Varimax norm curve calculated from A, with migration velocities from 0.1-0.3 m/ns. The optimal focusing velocity corresponds to the peak of the varimax norm curve. (C) Diffraction migrated with velocity of 0.2 m/ns. (D) Diffraction migrated with velocity of 0.15 m/ns. Note how the energy is much more tightly focused in C compared to D.

As with many geological materials, we assume the stratigraphic layers in snow are horizontal, so the RMS velocity at a given two-way travel time will be the same, regardless of horizontal position. This approximation will not be true over long transects, but data can be partitioned and processed in shorter lengths where this approximation will hold. Rather than attempting to isolate individual diffractions, we partition the radargram along the time axis and calculate the varimax norm of each subpartition. This approach is quicker than identifying and focusing individual diffractions, with similar accuracy.

2.2.2 Dix Inversion

For layered velocity media, the RMS velocity at the i^{th} interface is

$$(v_{rms}^i)^2 = \frac{\sum\limits_{j=0}^{i}(v_{int}^j)^2 \Delta t_j}{\sum_{j=0}^{i} \Delta t_j}, \tag{2.25}$$

where Δt_j is the two-way travel time spent in the j^{th} layer. For aerial GPR surveys, the medium will always be layered because the uppermost layer is air, with a radar velocity of 0.3 m/ns, while the true subsurface may have a radar velocity ranging from 0.25 m/ns (light snow) to 0.03 m/ns (water). With knowledge of the depths and velocities in overlying layers, the true velocity of a layer can be determined. This will not always be the case, but the velocity of air is known, and the radar reflection off the snow surface will be the first signal measured after the direct wave from transmitter to receiver. The height of the survey platform can thus be calculated for each trace. With this information, the layer interval velocities can be calculated recursively using Dix inversion [31]:

$$v_{int}^i = \sqrt{\frac{(v_{rms}^i)^2 t_i - \sum\limits_{j=1}^{i-1}(v_{int}^j)^2(t_j - t_{j-1})}{t_i - t_{i-1}}}, \tag{2.26}$$

where v_{int}^i is the interval velocity of the layer at time t_i, v_{rms}^i is the RMS velocity of the ith diffraction, t_j is the two-way travel time to the bottom of the j^{th} layer, and t_{i-1} is the two-way travel time to the top of the i^{th} layer. The uncertainty δ_{int}^i of the interval velocity can be calculated from the i^{th} diffraction:

$$\delta_{int}^i = \sqrt{\frac{(v_{rms}^i t_i \delta_{rms}^i)^2 + \sum\limits_{j=1}(v_{int}^j(t_j - t_{j-1})\delta_{int}^j)^2}{(v_{rms}^i)^2 t_i - \sum\limits_{j=1} v_{int}^j(t_j - t_{j-1})}} \tag{2.27}$$

where δ_{rms}^i is the uncertainty of the RMS velocity of the diffraction and δ_{int}^j is the uncertainty of the j^{th} interval velocity.

Rather than solving for the interval velocity corresponding to each (v_{rmsi}, t_i) pair, we use a non-linear curve fitting function to find the interval velocity that produces the RMS velocity curve of best fit for all pairs in each layer. The standard errors recovered with equation 2.24 are used to weight each pair. The interval velocities of lower layers are calculated sequentially.

2.2.3 SWE Recovery

We use diffraction analysis to determine the real part of the permittivity and the peak frequency shift method described by Bradford et al. [24] to determine the imaginary permittivity of the snow. The peak frequency shift method recovers frequency-dependent attenuation information from zero-offset GPR data by comparing the peak frequency in the snow surface reflection to that in the the snow-ground interface reflection. The first step is to determine the interval velocities in the snow using equation 2.26 if necessary, and the snow depth $z = v_{int}\frac{t}{2}$. With the snow velocity, ε' can be estimated using equation 1.1. The standard error of ε' is

$$\delta^i_{\varepsilon'} = \frac{2\delta^i_{int}}{\mu_0 v^3}. \tag{2.28}$$

The next step involves spectral analysis of the reflected pulses. Bradford derived the relationship between Q^*, a constant that describes the frequency-dependent attenuation of a radar pulse, and the spectral peak shift [32]

$$\frac{1}{Q^*} = \frac{2}{\pi t}\frac{f_0^2 - f_t^2}{f_0^2 f_t} \tag{2.29}$$

and the associated uncertainty

$$\delta_{Q^*} = \frac{\pi t}{2(f_0^2 - f_t^2)^2}[2f_t^3 f_0 \delta_{f_0} + f_0^2(f_0^2 + f_t^2)\delta_{f_t}]. \tag{2.30}$$

Q^* is defined in terms of the complex permittivity as

$$Q^* = \frac{\varepsilon'}{2\varepsilon''} \tag{2.31}$$

with uncertainty

$$\delta_{\varepsilon''} = 1/2[Q^*\delta_{\varepsilon'} + \varepsilon'\delta_{Q^*}], \tag{2.32}$$

where f_0 and f_t are the peak frequencies of the pulses reflected from the top and bottom of a layer, respectively, and t is the difference in arrival times between the two pulses. To determine f_0 and f_t, a Ricker wavelet spectral amplitude is fitted to the zero-phase spectrum, and the peak frequency is determined from the fitting parameters. The frequency uncertainties are taken from the fit parameter variances. The uncertainties in Q^* must not be considered in context: because equation 2.29 has a singularity at $f_0 = f_t$, a similar singularity exists in equation 2.30. Both of these equations are non-linear when $f_t \approx f_0$, so the derivative approach to error calculation is invalid in these regimes.

Given f_0 and f_1, Q^* can be calculated from Equation 2.29. With Q^* and ε' from the velocity analysis, ε'' can be calculated from Equation 2.31. Equation 2.32 gives the uncertainty estimate for ε''. With both components of the complex permittivity known, Equation 2.17 can be inverted to solve for ρ_d and W:

$$W = \frac{Im(\sqrt{\varepsilon' + \varepsilon'' i})}{Im(\sqrt{\varepsilon_w^*})} \tag{2.33}$$

$$\rho_d = \frac{\rho_{ice}}{\sqrt{\varepsilon_{ice}} - 1}\left[Re(\sqrt{\varepsilon' + \varepsilon'' i} - W\sqrt{\varepsilon_w^*} + W - 1\right] \tag{2.34}$$

where $Re(z)$ and $Im(z)$ denote respectively the real and imaginary parts of a complex-valued z. The uncertainties for W and ρ_d are

$$\delta_W = \frac{Im(\frac{\delta_{\varepsilon'} + i\delta_{\varepsilon''}}{2\sqrt{\varepsilon' + i\varepsilon''}})}{Im(\sqrt{\varepsilon_{water}^*})} \tag{2.35}$$

$$\delta_{\rho_d} = \frac{\rho_{ice}}{\sqrt{\varepsilon_{ice}} - 1}\left[Re(\frac{\delta_{\varepsilon'} + i\delta_{\varepsilon''}}{2\sqrt{\varepsilon' + i\varepsilon''}}) + \delta_W(1 - Re(\sqrt{\varepsilon_{water}^*}))\right]. \tag{2.36}$$

Once the values of ρ_d and W are known for each layer, one can estimate the total SWE and uncertainty,

$$SWE = \sum_i (\rho_{d_i} + W_i)\Delta z_i = \sum_i (\rho_{d_i} + W_i)\frac{\Delta t_i v_i}{2} \tag{2.37}$$

$$\delta_{SWE} = \sum_i \frac{\Delta t_i}{2}\left[v_i(\delta_{\rho_{d_i}} + \delta_{W_i}) + (\rho_{d_i} + W_i)\delta_{int_i}\right]. \tag{2.38}$$

CHAPTER 3
MODEL VALIDATION

3.1 Model

To determine the liquid water content of snow from GPR data, we rely on the linearity of the frequency-dependent attenuation in the GPR bandwidth, as demonstrated empirically by Turner and Siggins [33]. To show that the forward model developed by Bergmann et al. [25] is consistent with the empirical data produced by Turner and Siggins, we created a one-dimensional model simulating 0.5 m of fresh water with an aluminum plate at the bottom. The values of $\tau_E = 3.44 \times 10^{-13}$ s, $\tau_D = 9.3 \times 10^{-12}$ s, $\varepsilon_s = 79.77$, and $\sigma_w = 0.001$ S/m were taken from Turner and Siggins for pure water at 20°C. The conductive plate was modeled by changing the conductivity at depths below 0.5 m to $\sigma_a = 10,000$ S/m. The model was discretized with $\Delta z = 1 \times 10^{-5}$ m and propagated with $\Delta t = 4.71 \times 10^{-15}$ s. To reduce edge effects, the conductivity profile was convolved with a Gaussian kernel with a standard deviation of 51 units. Although we could not find waveform data to accurately reproduce the transmitter signal of the GSSI Model 101C 900 MHz antenna used by Turner and Siggins, the frequency-attenuation characteristics are independent of the wavelet used, as long as the frequency bands are in a similar range. For a source wavelet, we use a Ricker wavelet with a 900 MHz center frequency. The source wavelet is injected in the time domain, as described in detail in Section 4.1.4.

3.2 Results

Because of issues associated with perfectly reproducing the source signal of a particular instrument coupled to a non-air medium, we could not perfectly reproduce the exact wave forms observed by Turner [33]. However, the modeled signals exhibit the same broadening and amplitude attenuation with increasing path length that is present in the empirical signals (Figure 3.1).

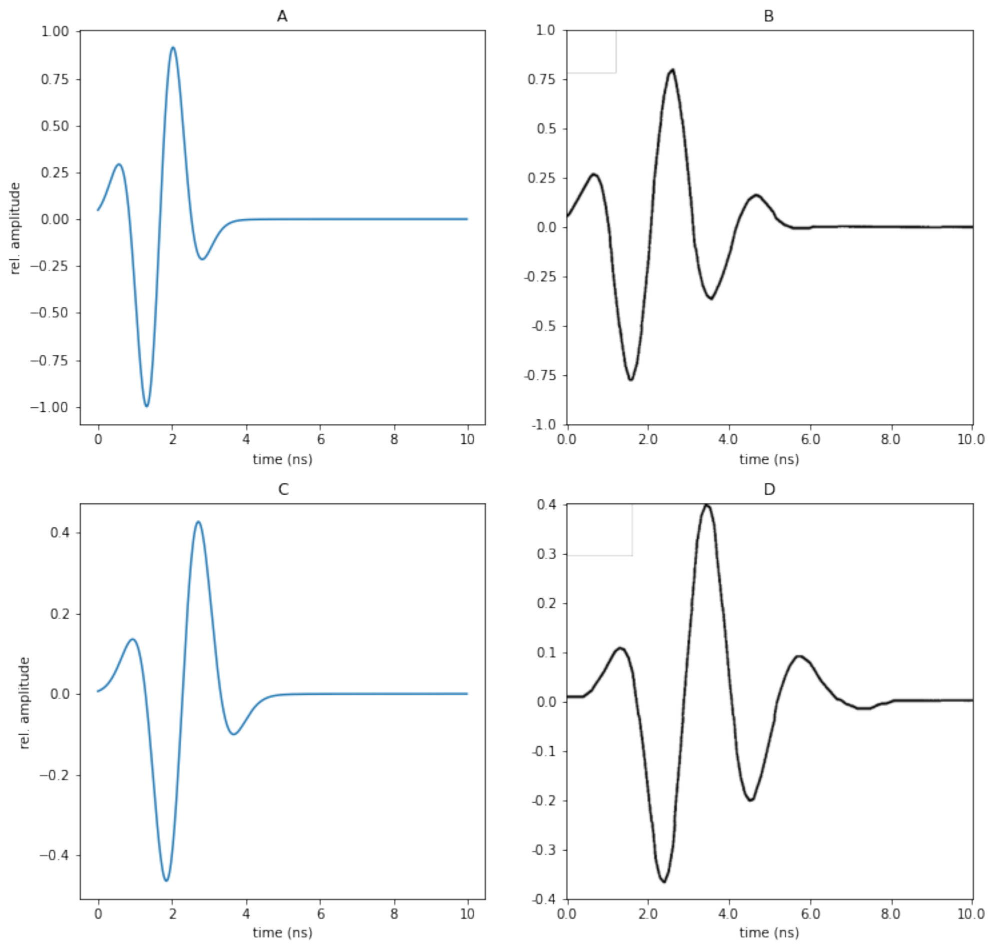

Figure 3.1: Modeled and empirical radar reflection signals from aluminum sheet in water. Empirical signals from Turner and Siggins [34]. (A) Modeled signal with 0.6 m total travel path. (B) Empirical signal with total 0.6 m travel path. (C) Modeled signal with 1.0 m total travel path. (D) Empirical signal with 1.0 m total travel path.

More importantly, Figure 3.2 shows that the shift in peak frequency between the modeled signals are close to the same value as observed by Turner and Siggins. Though they do not give the precise values of the peak spectral frequencies, the peak frequencies for the 0.6 m and 1.0 m signals are approximately 500 MHz and 410 MHz, respectively. Consequently, $\Delta f \approx 90MHz$. For the modeled signals, the peak frequencies are 571 MHz and 471 MHz for the 0.6 m and 1.0 m signals, respectively, giving $\Delta f = 100$ MHz. Because the goal of the forward model is to reproduce the frequency-dependent attenuation, measured by the shift in the peak spectral frequency, the closeness of the empirical and modeled frequency shifts corroborates the accuracy of our forward model for capturing frequency-dependent attenuation.

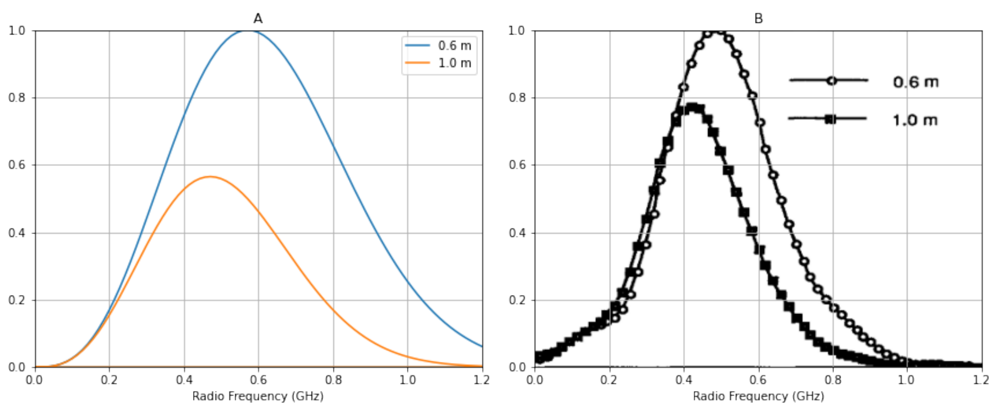

Figure 3.2: Modeled and empirical spectra of radar reflection signals from an aluminum sheet in water with travel paths of 0.6 and 1.0 m. (A) Modeled spectra, normalized to peak spectral amplitude of 0.6 m signal. (B) Empirical spectra, normalized to peak spectral amplitude of 0.6 m signal.

CHAPTER 4

SYNTHETIC CASE STUDY

4.1 Model Creation

To simulate GPR data collected from an aerial platform, we generated four synthetic models, each consisting of four two-dimensional arrays of permittivity, conductivity, and relaxation times. The models were generated assuming a layer of air over a layer of snow with internal layering to allow for varying density and wetness underlain by unfrozen, homogeneous ground. The snow-ground interface is variable and is based on snow depth field data collected in the Arctic [35]. Figure 4.1 shows permittivity, conductivity, and relaxation time images for each model used to generate synthetic radar data. Model 1 is a homogeneous, dry snow with $\rho_d = 0.3$ g/cm^3. Model 2 is a homogeneous wet snow with $\rho_d = 0.3$ g/cm^3 and $W = 0.1$. Model 3 is a two-layered dry snow model with $\rho_d = 0.25, 0.45$ g/cm^3. Model 4 is a two-layered wet snow model with $\rho_d = 0.25, 0.45$ g/cm^3 and $W = 0.0, 0.1$.

4.1.1 Discretization and Instability

The discretization increments for the x and z directions were kept the same and chosen using

$$\Delta x = \frac{\lambda_{min}}{10} = \frac{c\sqrt{\varepsilon_{s,max}}}{10 f_{max}} \tag{4.1}$$

where $\varepsilon_{s,max}$ is the maximum static permittivity in the model and f_{max} is the maximum frequency of the source wavelet to be captured. Although the frequency spectrum of a Ricker wavelet only approaches zero as $f \to \infty$, the frequency components above $2.2f_0$ are negligible. Therefore, we assume $f_{max} = 2.2f_0$, where f_0 is the center frequency of the wavelet. For all 2D models, $\Delta x = \Delta z = 0.004228457$ m. The temporal discretization increment was calculated using the CFL criterion:

$$\frac{c}{\sqrt{\varepsilon_{max}}}\Delta t(\frac{1}{\Delta x} + \frac{1}{\Delta z}) \leq 1.0. \tag{4.2}$$

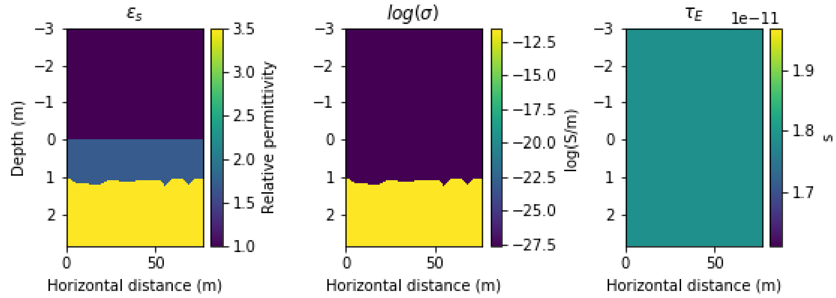

(a) Model 1

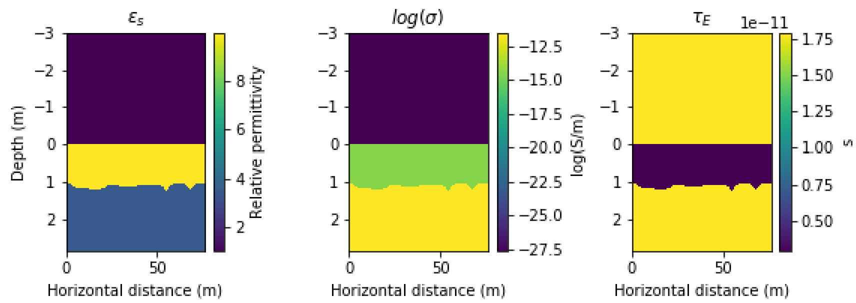

(b) Model 2

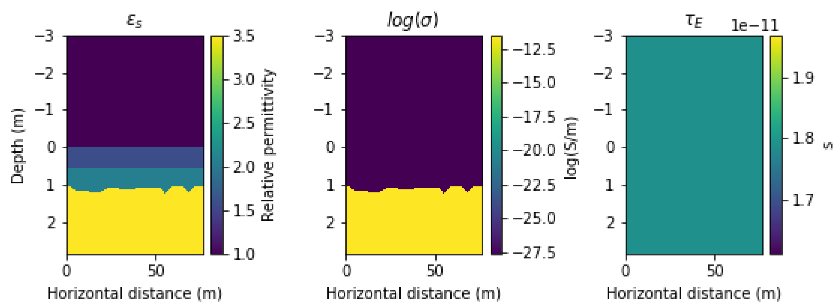

(c) Model 3

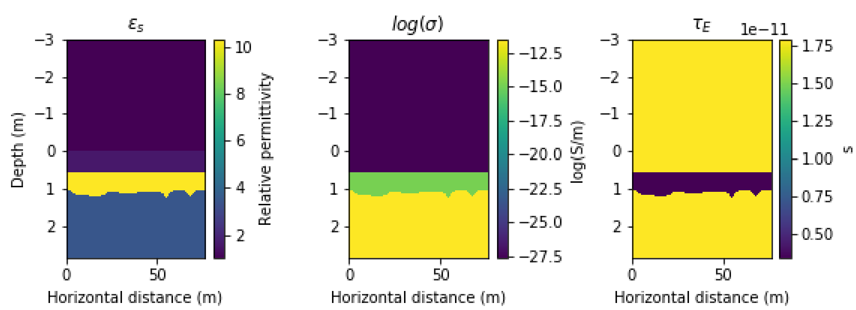

(d) Model 4

Figure 4.1: Static permittivity, conductivity, and relaxation time images for Models 1-4.

For all models, the discretization increments yielded by equations 4.1 and 4.2 result in a stable solution to Equations 2.8-2.11.

4.1.2 Absorbing Boundaries

To minimize the computational domain necessary while eliminating reflection artifacts, we added a layer of width $n = 4\frac{c}{f_0 \Delta x}$ around all four edges of the computational domain. Within this layer the conductivity increases exponentially according to

$$\sigma(x) = (\sigma_0 + 0.0003\frac{S}{m})e^{x/\beta}, \tag{4.3}$$

where σ_0 is the conductivity value immediately adjacent to the beginning of the absorbing boundary layer and β is the growth rate. By trial and error, $\beta = \frac{c}{2f_0}$ was determined to optimally absorb incident waves without generating reflections at the boundary. Figure 4.2 shows the conductivity image for Model 1 after the absorbing boundary layer is generated.

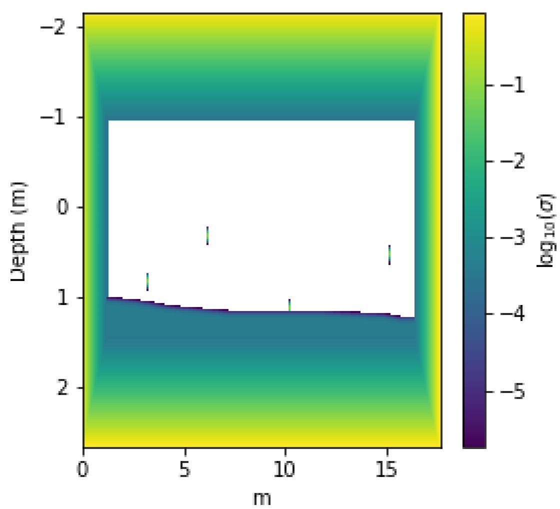

Figure 4.2: The conductivity image used to generate data for Model 1. White spaces denote a conductivity of 0.0. The absorbing conductivity layer begins 1.17 m from each edge and increases exponentially, following Equation 4.3. The absorbing boundaries are generated similarly for each model.

4.1.3 Synthetic Diffractions

Although diffractions will be produced from sharp corners at interfaces, this will only produce diffractions at the snow-ground interface in our model. To increase the number of diffractions, and to ensure that diffractions are present in the upper layers of heterogeneous models, we artificially introduce four high-conductivity points at the same locations in each model: two in the upper half of the snow and two in the lower half and horizontally distributed. Such diffractions may be caused in field data by the presence of rocks, sticks or voids in the snow. Without intra-snow diffractions present in GPR data, Dix inversion of layered snow is not possible.

4.1.4 Source Injection

For an electromagnetic wave with angular frequency ω propagating in a material with absolute permittivity ε, conductivity σ, and magnetic permeability μ, the complex wave number $\tilde{k}$ is given by [36]

$$k^* = k' + ik" \tag{4.4}$$

where

$$k' = \omega\sqrt{\frac{\varepsilon\mu}{2}}\left[\sqrt{1+\left(\frac{\sigma}{\varepsilon\omega}\right)^2}+1\right]^{1/2}$$
$$k" = \omega\sqrt{\frac{\varepsilon\mu}{2}}\left[\sqrt{1+\left(\frac{\sigma}{\varepsilon\omega}\right)^2}-1\right]^{1/2}.$$

The reflectivity R_i for normal incidence at a layer interface is

$$R_i = \frac{\frac{\omega\mu_i}{k_i^*} - \frac{\omega\mu_{i+1}}{k_{i+1}^*}}{\frac{\omega\mu_i}{k_i^*} + \frac{\omega\mu_{i+1}}{k_{i+1}^*}}. \tag{4.5}$$

For most geologic materials, the magnetic permeability has little variation, so $\mu_i \approx \mu_0$ and thus

$$R_i = \frac{\frac{1}{k_i^*} - \frac{1}{k_{i+1}^*}}{\frac{1}{k_i^*} + \frac{1}{k_{i+1}^*}} \tag{4.6}$$

$$R_i = \frac{k_{i+1}^* - k_i^*}{k_{i+1}^* + k_i^*}. \tag{4.7}$$

The source wavelet of most GPR systems can be approximated by a Ricker wavelet. For our models, we used a Ricker wavelet with center frequency $f_0 = 1$ GHz calculated over a range of times t. Figure Figure 4.3 shows the initial wavelet used for each model.

Equation 4.8 shows the modified variation of equation 2.11 used to inject a source wavelet as a function of time, where S^n is the value of the source function at time step n and $R_{x,z}$ is the value of the reflectivity at location (x, z):

$$\begin{aligned} E_{y_{x,z}}^{n+1} = E_{y_{x,z}}^{n} + \frac{\Delta t}{\varepsilon_\infty^e}[&\frac{-H_{x_{x,z+3/2}}^{n+1/2} + 27H_{x_{x,z+1/2}}^{n+1/2} - 27H_{x_{x,z-1/2}}^{n+1/2} + H_{x_{x,z-3/2}}^{n+1/2}}{24\Delta z} \\ &- \frac{-H_{z_{x+3/2,z}}^{n+1/2} + 27H_{z_{x+1/2,z}}^{n+1/2} - 27H_{z_{x-1/2,z}}^{n+1/2} + H_{z_{x-3/2,z}}^{n+1/2}}{24\Delta x} \\ &- \sigma_\infty^e(E_{y_{x,z}}^{n+1} + E_{y_{x,z}}^{n}) - \varepsilon_s m_{x,z}^{n+1/2} + S^n R_{x,z}]. \end{aligned} \tag{4.8}$$

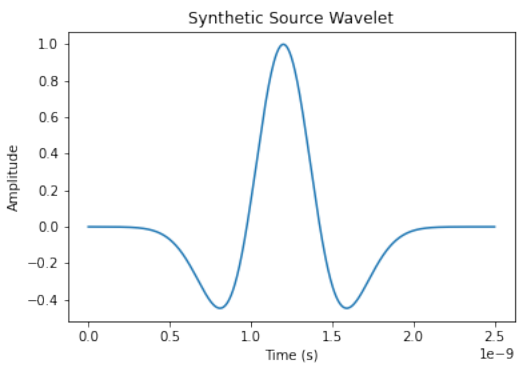

Figure 4.3: Initial wavelet injected into each model. The wavelet is a Ricker wavelet with center frequency of 1 GHz.

4.2 Exploding Reflector Model

Utilizing an exploding reflector model reduces substantially the computational requirements for modeling zero-offset data that would be collected from an aerial platform. The exploding reflector model replaces two-way travel from the source to receiver with one-way travel from reflecting interfaces to the receiver location. The radar velocity [36]

$$v = \frac{1}{\sqrt{\mu_0 \varepsilon'}} = \frac{1}{\sqrt{\mu_0 \varepsilon_s \frac{\tau_E}{\tau_D}}} \tag{4.9}$$

and the total attenuation A [25, 34]

$$A(z) = A_0 e^{-\frac{\omega z}{2vQ^*}}, \tag{4.10}$$

where

$$Q^* = \frac{\frac{1+\omega^2\tau_D\tau_E}{1+\omega^2\tau_D^2} + \frac{\sigma_s}{\varepsilon_s}\tau_\sigma}{\frac{\omega(\tau_D-\tau_E)}{1+\omega^2\tau_D^2} + \frac{\sigma_s}{\varepsilon_s\omega}}, \tag{4.11}$$

of a medium determine the travel-time and attenuation characteristics of a radar signal propagating through the medium.

By replacing two-way travel with one-way travel, we halve the travel distance: $z' = \frac{z}{2}$. To maintain a consistent travel time, we must also halve the velocity:

$$\begin{gathered} v' = \frac{v}{2} \\ \frac{1}{\sqrt{\mu_0' \varepsilon_s' \frac{\tau_E}{\tau_D}}} = \frac{1}{2\sqrt{\mu_0 \varepsilon_s \frac{\tau_E}{\tau_D}}}. \end{gathered} \tag{4.12}$$

To determine how the quality factor Q^* must be adjusted to maintain consistent attenuation, we set the two-way and one-way attenuation values, A and A', to be equal:

$$
\begin{aligned}
A(2z) &= A'(z) \\
A_0 e^{-\frac{\omega 2z}{2vQ^*}} &= A_0 e^{-\frac{\omega z}{2\frac{v}{2}Q^{*\prime}}} \\
e^{-\frac{\omega z}{vQ^*}} &= e^{-\frac{\omega z}{vQ^{*\prime}}} \\
\frac{\omega z}{vQ^*} &= \frac{\omega z}{vQ^{*\prime}} \\
Q^* &= Q^{*\prime} \\
\frac{\frac{1+\omega^2\tau_D\tau_E}{1+\omega^2\tau_D^2} + \frac{\sigma_s}{\varepsilon_s}\tau_\sigma}{\frac{\omega(\tau_D-\tau_E)}{1+\omega^2\tau_D^2} + \frac{\sigma_s}{\varepsilon_s\omega}} &= \frac{\frac{1+\omega^2\tau_D\tau_E}{1+\omega^2\tau_D^2} + \frac{\sigma_s'}{\varepsilon_s'}\tau_\sigma}{\frac{\omega(\tau_D-\tau_E)}{1+\omega^2\tau_D^2} + \frac{\sigma_s'}{\varepsilon_s'\omega}}.
\end{aligned} \tag{4.13}
$$

To satisfy equations 4.12 and 4.13, we use updated permittivity and conductivity values

$$
\begin{aligned}
\varepsilon_s' &= 4\varepsilon_s \\
\sigma_s' &= 4\sigma_s.
\end{aligned} \tag{4.14}
$$

Thus, the only change that must be made to our domain parameters is scaling by four the static permittivity and conductivity. This transformation of the material parameters should accurately reproduce the travel times and attenuation characteristics.

4.3 Noise

To more accurately simulate field data, we injected normally distributed, random noise into the synthetic data prior to analysis. This produces random noise over the full bandwidth of the signal. The standard deviation of the noise was calculated from the mean power of the first reflection in the clean data so that the signal-to-noise ratio for each radargram was 10 dB at 7 ns.

CHAPTER 5

RESULTS

5.1 Modeling

To simulate collection from an aerial platform, the value of the wavefield is recorded at a constant height of 1.0 m above the snow surface. A time step of $\Delta t = 1.35 \times 10^{-13}$ s was used for forward modeling of the wavefield and the signal was downsampled to a sampling period of 5×10^{-11} s. Figure 5.1 shows the 2D radargrams prior to the processing steps outlined in Section 2.2. Figure 5.2 shows the radargrams after a local background subtraction is applied, emphasizing the diffractions necessary for common-offset velocity analysis. Figure 5.3 shows sample ground-reflected wavelets from Model 1 and Model 2, with noise added.

5.2 Velocity Analysis

Figure 5.4 shows the true layer interval velocities for each model, as well as the final estimates and the standard error estimate for each estimate. The average relative error in the velocity estimates was 12.7%.

5.3 Frequency Analysis

Figure 5.5 shows the spectral content of the specular reflections for each model. Table 5.1 gives representative peak frequencies for the top and bottom reflections for each model and layer, the two-way travel time in each layer, and the values of Q^*. Because the bottom layer has variable thickness, and consequently travel times, we summed the spectral content of adjacent traces in 1.0 m increments, calculated Q^* from these averaged traces, and took the median value of Q^* and the associated uncertainty.

Table 5.1: Representative best fit peak frequencies, two-way travel times, and Q^* for specular reflections in each model. Q^* is not calculated for the air layers: this is assumed to be ∞.

Model	Layer	$f_0 \pm \delta_{f_0}$ (GHz)	$f_t \pm \delta_{f_t}$ (GHz)	Δt (ns)	$Q^* \pm \delta_{Q^*}$
1		1.003 ± 0.003	1.001 ± 0.025	10.3	4491.7 ± 145327.6
2		0.985 ± 0.015	0.531 ± 0.052	14.5	15.5 ± 2.5
3	A	1.004 ± 0.036	1.005 ± 0.046	4.9	-3358.3 ± 239021
3	B	1.005 ± 0.046	1.001 ± 0.026	5.7	1252.7 ± 25143.5
4	A	1.001 ± 0.025	0.983 ± 0.017	4.9	225.5 ± 458.0
4	B	0.983 ± 0.017	0.695 ± 0.048	7.6	13.4 ± 2.5

5.4 SWE Analysis

Using Equations 2.31, the complex permittivity of the snow in each model was calculated. The values of ρ_d and W were calculated for each model using 2.34, and 2.33. Figure 5.6 shows the permittivity components, ρ Then the SWE of each layer was calculated using Equation 2.37. The true SWE values and the SWE values estimated from the data are shown in Figure 5.7. The average relative error in the SWE estimates is 11.0% and the maximum relative error is 26.8% in Model 4.

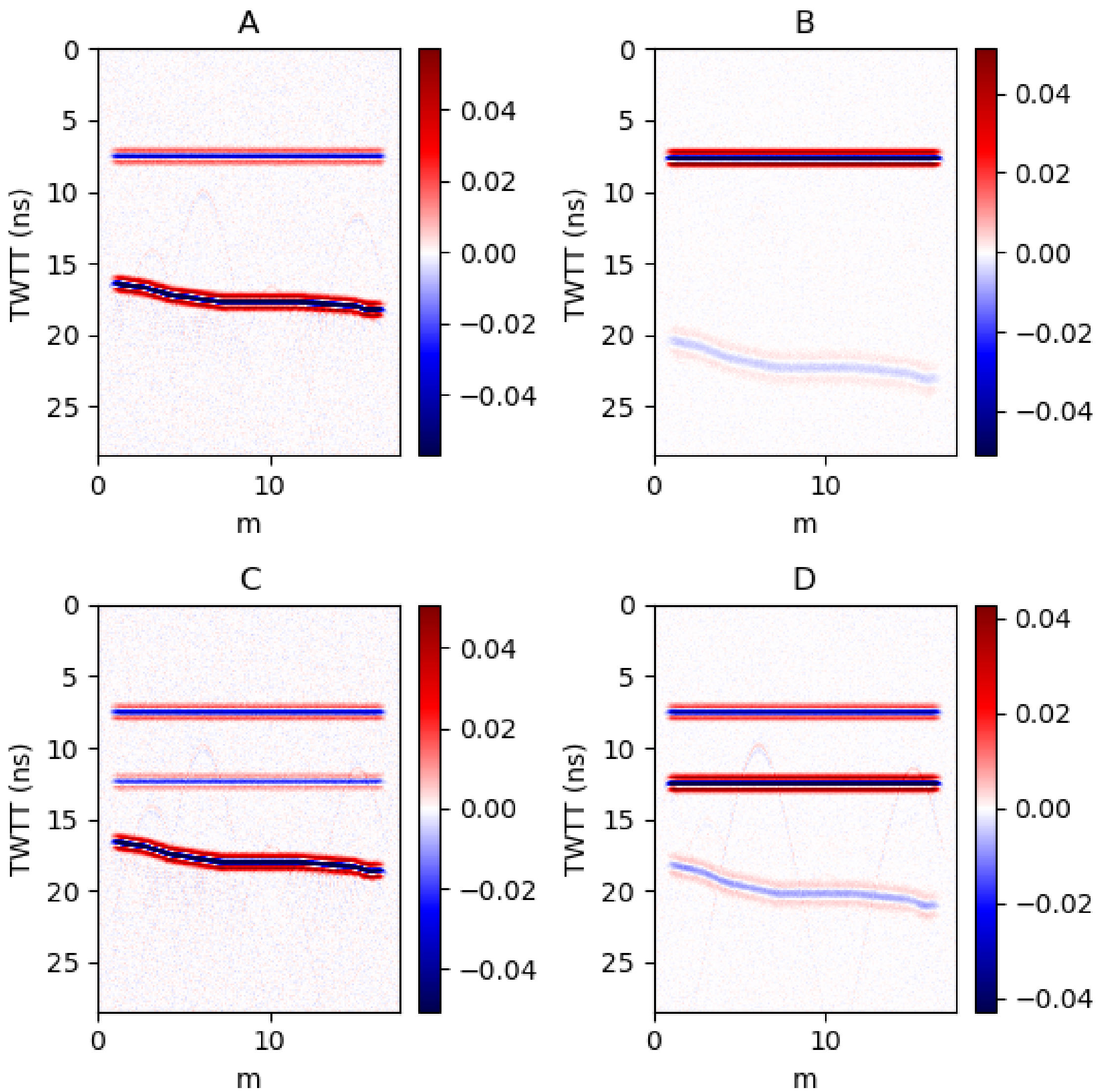

Figure 5.1: Pre-processed radargrams with noise for Model 1 (A), Model 2 (B), Model 3 (C), and Model 4 (D). Prior to background subtraction, the specular reflections from the interfaces dominate the signal.

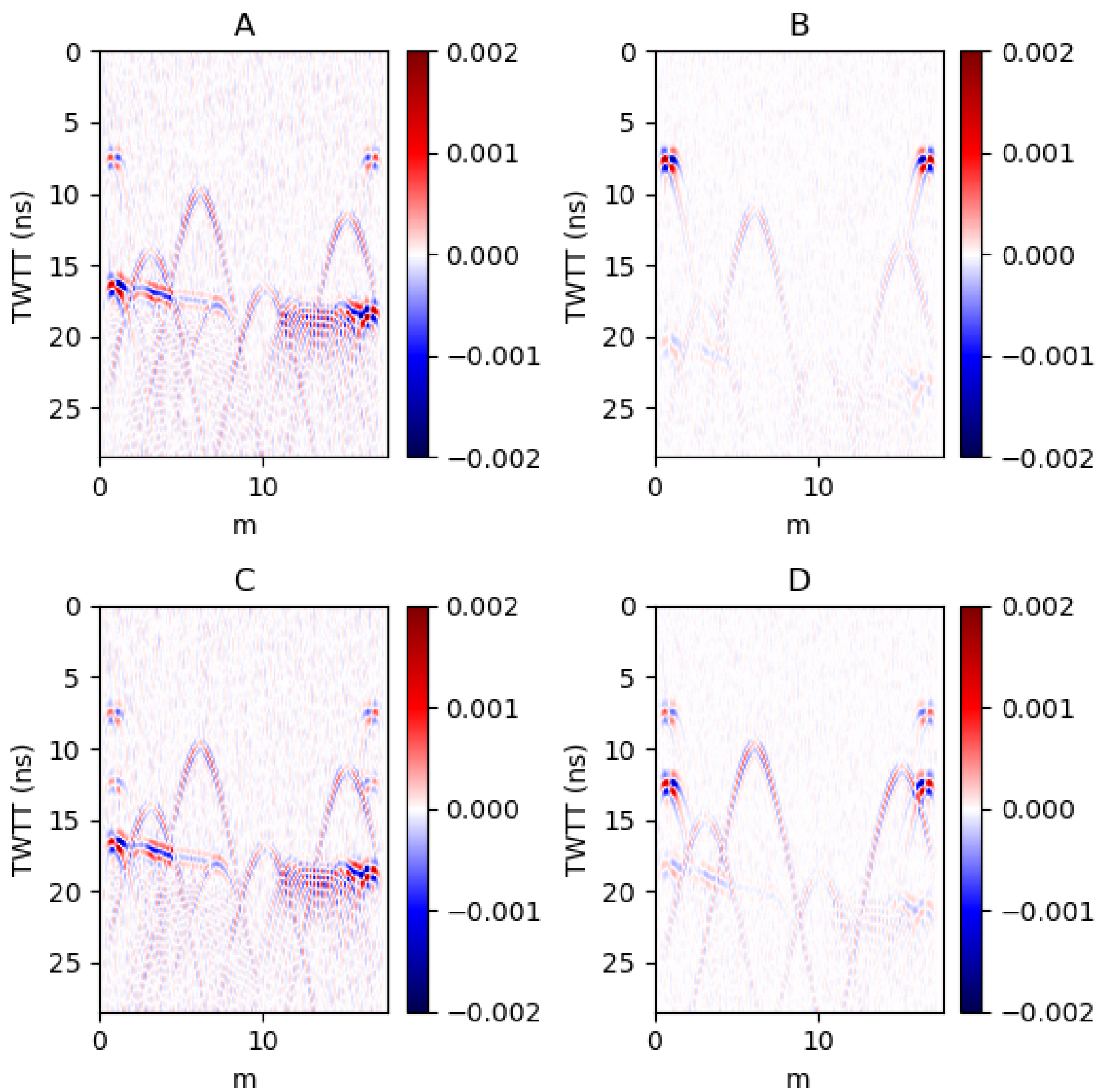

Figure 5.2: Background-subtracted radargrams for Model 1 (A), Model 2 (B), Model 3 (C), and Model 4 (D). The localized background subtraction largely eliminates the specular reflections at all but the steepest dip angles, emphasizing the diffraction signals necessary for velocity analysis.

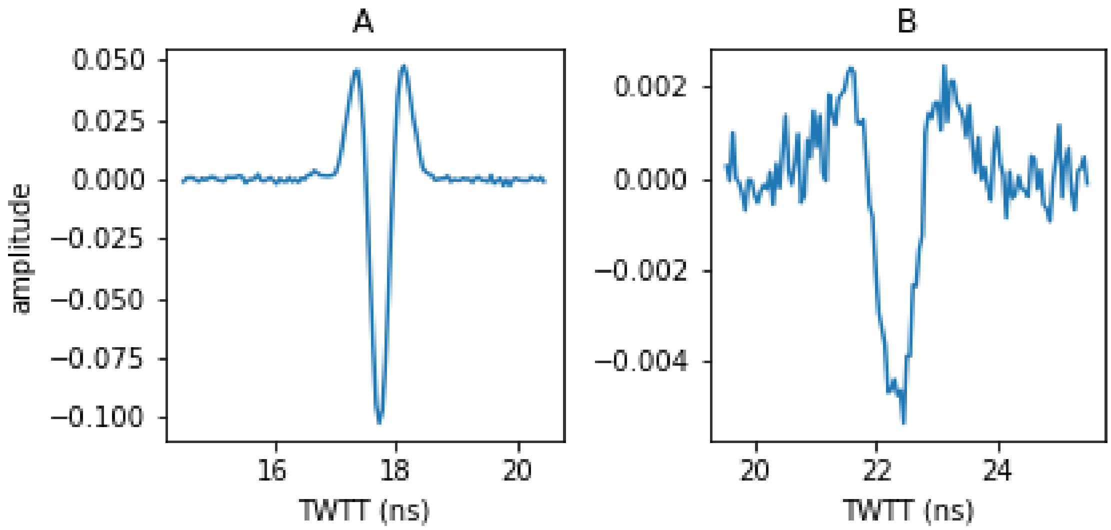

Figure 5.3: (A) Ground-reflection wavelet at 10.1 m from Model 1. (B) Ground-reflected wavelet at 10.1 m from Model 2. Broadening is observable in the wavelet that has traveled through wet snow (B) compared to a wavelet traveling the same path through dry snow (A).

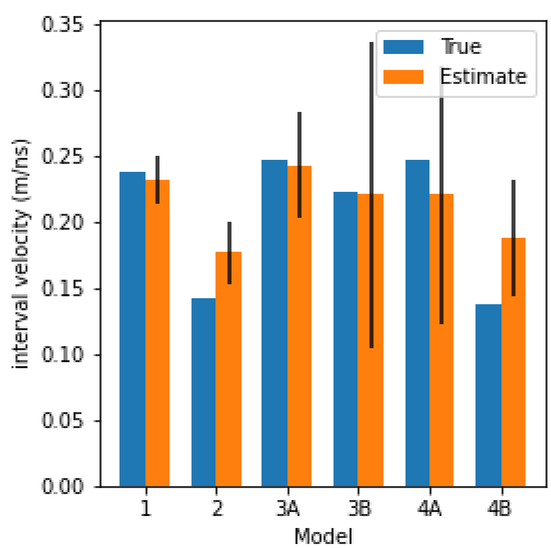

Figure 5.4: True interval velocities and estimates from diffraction analysis. A and B refer to the upper and lower layers, respectively.

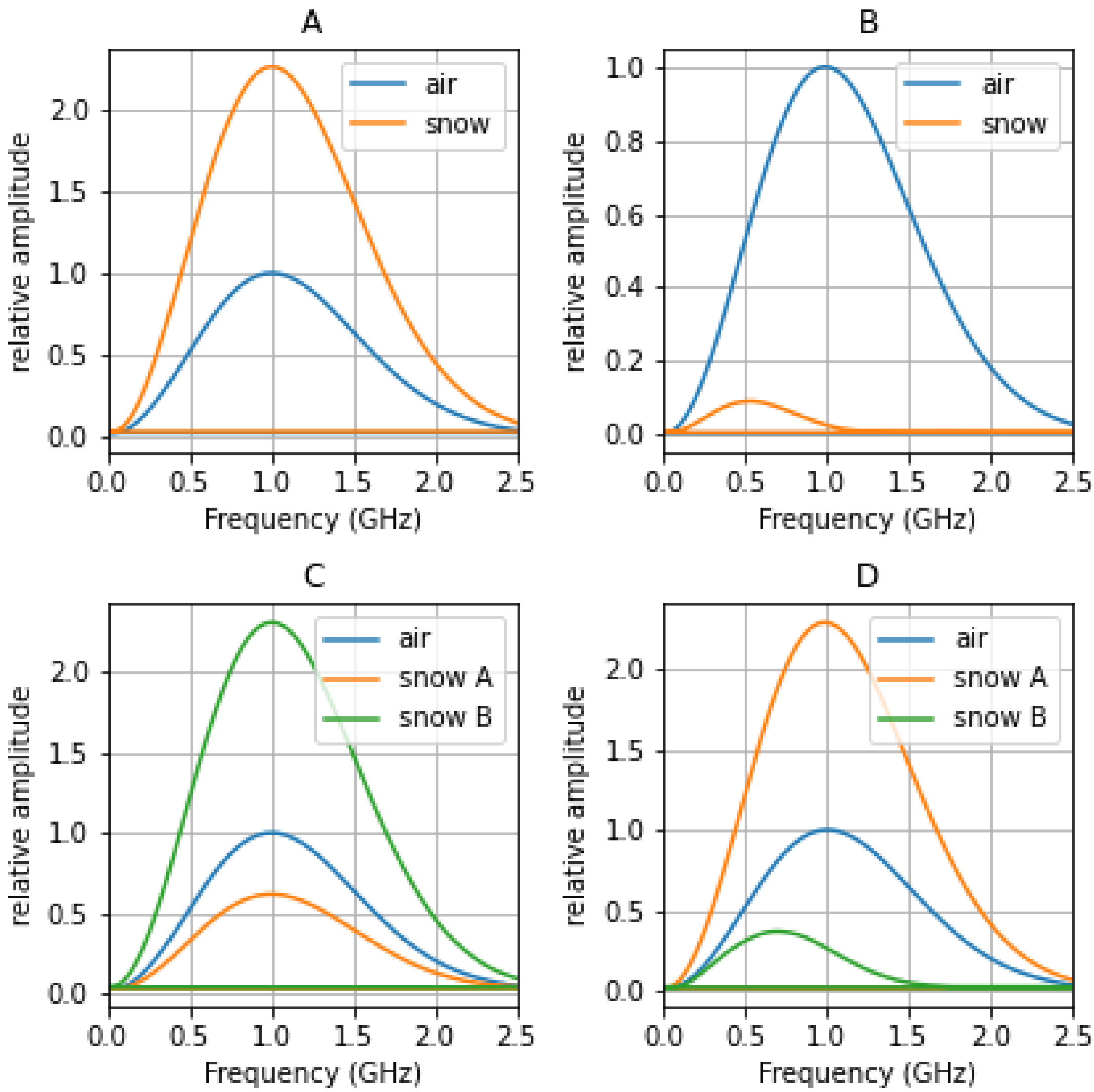

Figure 5.5: Average spectral content of specular reflections for (A) Model 1, (B) Model 2, (C) Model 3, and (D) Model 4. Notable frequency-dependent attenuation is observable only in the "wet" layers - Model 2 and Model 4B.

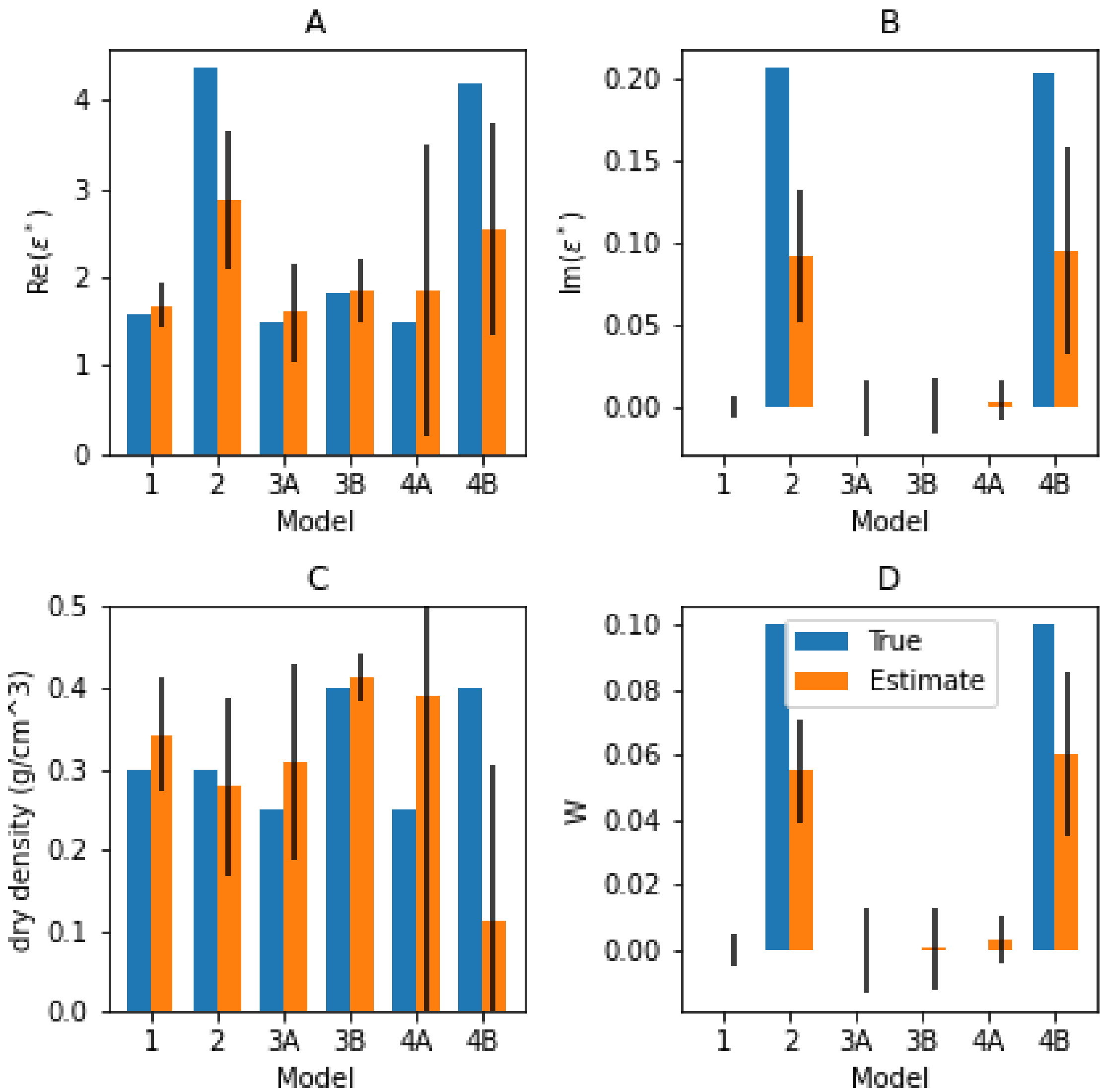

Figure 5.6: (A) True and estimated real permittivities. (B) True and estimated imaginary permittivities. (C) Dry snow density and (D) volumetric water content calculated from complex permittivity values.

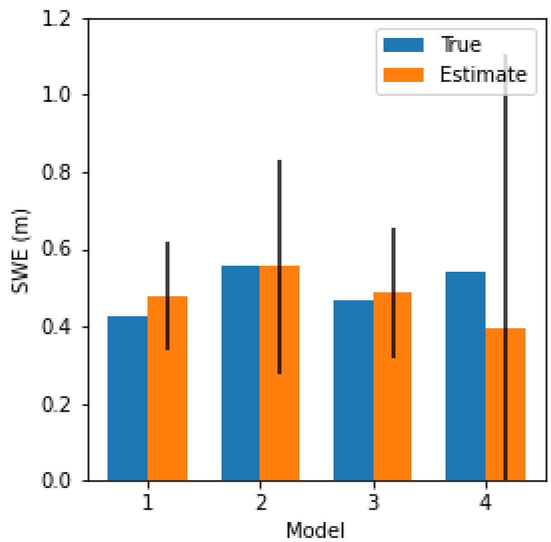

Figure 5.7: True and estimated total SWE for each model.

CHAPTER 6

DISCUSSION AND CONCLUSIONS

The purpose of our research was to develop a workflow for modeling and analysis of aerial GPR data collected over wet and snow. Common-offset GPR surveys are fast to acquire and are an attractive platform for targeted snowpack surveys in areas that may be too time-intensive or dangerous for ground-coupled surveys. Our wave propagation approach allows for the modeling of heterogeneous, laterally varying snow, which can support the development of new research in frequency-dependent attenuation analysis of GPR. The diffraction analysis methodology we used combines the specificity and customization of manual diffraction selection with the efficiency of bulk analysis. By integrating diffraction analysis with spectral analysis of reflected pulses, we are able to estimate SWE from synthetic common-offset GPR data. Our analysis workflow should be directly applicable to common-offset GPR data collected from aerial platforms. Here we discuss the accuracy of the method for recovering SWE and the various sources of error encountered and how we addressed them.

6.1 Sources of Error

Several sources of error were encountered, both with the modeling and analysis. Some, such as ringing and introduced noise, have relatively simple solutions. Others, like inconsistent migration velocity picks and bulk attenuation, are more difficult to mitigate and require additional research.

6.1.1 Ringing Artifacts

Ringing artifacts at sharp medium boundaries in finite-difference time-domain wave modeling are a recognized problem [37]. Various methods exist to minimize this acausal ringing, including solving the wave equation in the frequency domain. We opted to eliminate the sharp edges in the domain by convolving the permittivity, conductivity, and τ_E domains with a 1D Gaussian kernel with a standard deviation of 0.05 cm. Due to the narrow width of the kernel, the impact on the velocity and attenuation of the recorded signal is negligible.

6.1.2 Noise Mitigation

Normally distributed noise was added to the synthetic data prior to analysis. The presence of noise can impact the results of background-subtraction, Stolt migration, and spectral frequency analysis. To minimize the impact of the background noise, a time-domain lowpass filter was used to minimize frequencies above 2 GHz.

In the spectral analysis, we did not use filtered data. Instead, we improved the spectral signal-to-noise ratio by summing the respective zero-phase spectra for each interface in neighboring traces over 1.0 m intervals. Using this approach, we improved the spectral signal-to-noise ratio at the ground reflection in Model 2 from $\tilde{1}5$ dB for any given trace to 21 dB.

6.1.3 RMS Velocity Curve Fitting

For each model, the optimal migration velocity was calculated for each 1 ns strip of data between the air wave and the ground wave. However, this approach can produce a wide spread of migration velocity values that do not necessarily fit a smooth curve well. Figure 6.1 shows the varimax curves recovered from various depths, as well as the distribution of migration velocity picks, the RMS velocity curve that best fits the distribution, and the true RMS velocity curve for Model 4. The migration velocity picks are distributed relatively widely around the curve of best fit, increasing the uncertainty in the recovered interval velocities.

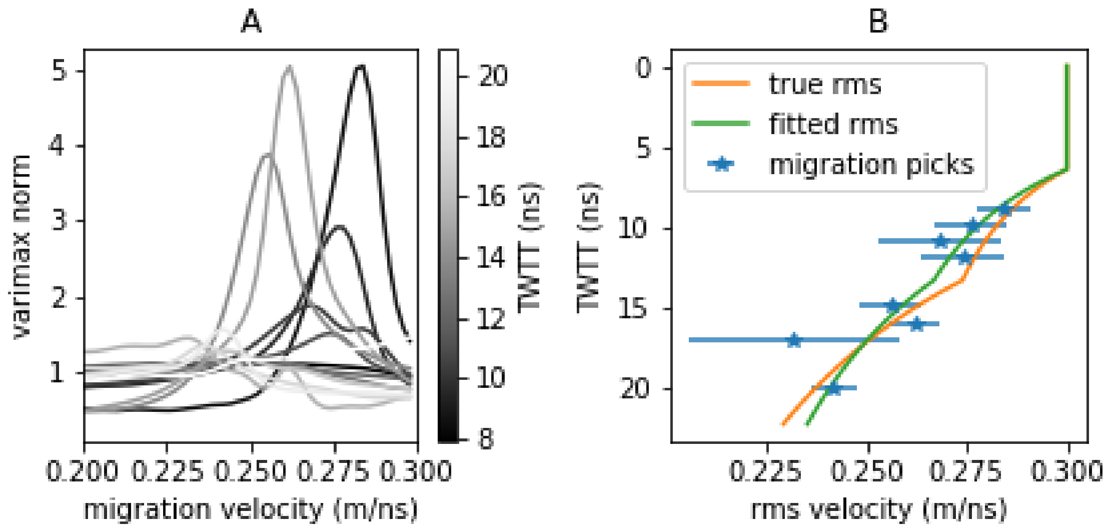

Figure 6.1: (A) Varimax norm curves 1 ns strips of data in Model 4. Darker colors correspond to shallower depths. The peak in each curve corresponds to the optimal migration velocity for focusing diffractions. (B) Blue asterisks with error bars denote the distribution of migration velocity picks with depth and uncertainties calculated from FWHM varimax peak widths. The orange curve denotes the true RMS velocity curve with depth, and green the RMS velocity curve fitted to the migration velocity picks.

6.1.4 Bulk Attenuation

Depth of investigation is a recognized limitation of GPR, and the depth of investigation decreases substantially with increasing conductivity, due to the attenuation of the signal. This attenuation is observable in the raw radargrams (Figure 5.1) and in the relative peak spectral magnitudes for the pulses traveling through dry snow compared to those through wet snow (Figure 5.5). This attenuation may explain the greater error and uncertainty in velocity estimates for Models 2 and 4, relative to Models 1 and 3 (Figure 5.4). One approach for mitigating this bulk attenuation is to use an inverse Q filter, as described by Irving and Knight [38]. Unfortunately, the success of this approach will be highly dependent on the spectral content of the noise obscuring the signal. If the noise has a higher frequency content than the signal, an inverse Q filter will amplify the noise more than the signal.

6.2 Results

Figure 5.7 shows the results of our SWE recovery method, compared to the true value of the synthetic model. Across all models, the mean error is 11.0%. This is comparable to the errors observed by others in GPR field data for dry snow [18]. The reported error observed with the most accurate field sampling method, the federal snow sampler, is 5-11% [39]. One area of concern lies in the magnitude of the uncertainty estimates for the final SWE values. The method of uncertainty determination and propagation we utilize is unique, so we cannot compare our values to other studies. St Clair and Holbrook assume a 95% confidence interval at 95% of the maximum varimax norm peak height [18]. This results in standard errors much smaller than those produced by calculating the standard error from the FWHM peak width. More research is required to ascertain which approach is more representative of the true uncertainty.

The errors in the values of ρ_d and W for the component layers of Models 3 and 4 (Figure 5.6) are larger than the errors in the total SWE for those same models (Figure 5.7). This is due to correction in iterative RMS velocity fitting. In layered media, we assume independent RMS velocities for each layer. When the RMS velocity is underestimated in an upper layer, the RMS velocity in lower layers will tend to be overestimated (Figure 6.1), and vice versa. This is due to the iterative implementation of Dix inversion. Consequently, while errors in the velocity estimates of individual layers may be large, the impact on final SWE estimates tend to be much smaller.

The application of diffraction analysis to common-offset GPR data relies on the presence of observable diffractions to recover the radar velocity. In most field conditions, the presence of uneven ground topography, rocks, or trees under the snow will provide sufficient diffractions for a relatively accurate velocity recovery [18]. When assuming a layered snowpack, the more probable issue is the lack of diffractors within each snow layer. Unfortunately, this is a physical limitation that cannot be solved through processing techniques. This issue could be mitigated by pairing limited common-midpoint surveys or snow depth probes on the ground with aerial common-offset surveys. We do not attempt to address survey design; our focus is specifically on the processing techniques necessary to recover SWE exclusively from an airborne platform.

6.3 Future Work

With an analysis workflow developed and proven on synthetic data, the next step is to collect field data. The integration of a GPR system with a UAS is not a simple process, but there are several companies which offer integrated systems [40–42]. With proven results from field data, aerial GPR can be deployed by water management agencies as a fast, safe, and accurate method for SWE surveys of long transects in wet snow conditions. The impacts of a lack of intra-layer diffractions in layered snow should be researched to provide an error estimate for field data that does not contain embedded diffractions in all observable layers.

6.4 Conclusion

Our approach to SWE estimation from common-offset GPR data advances beyond previous work in three important respects: rigorous uncertainty propagation, handling of stratified snow, and handling of wet snow. Previous work in the application of GPR to SWE calculation have not presented convincing methods for propagating uncertainties through each step of analysis. Our approach derives formulas to carry uncertainties through each step of analysis, providing a framework for future research to standardize uncertainty estimate calculations.

The utilization of diffraction analysis for determination of radar velocities in snow is not new. However, others have assumed that the snow velocity is constant. By calculating the optimal focusing velocity at various depths and fitting curves to the data, we show it is possible to calculate the interval velocities of horizontal layers quickly, increasing the accuracy of total SWE calculations.

Finally, our approach handles partially melted snow. By integrating spectral shift analysis with diffraction analysis, sufficient information can be recovered from common-offset GPR data to fully recover complex permittivity, and consequently SWE for both wet and dry snow. Because liquid water is common in snowpack at peak SWE when snow surveys are most valuable, our approach makes GPR more useful for snow surveyors.

We were able to recover the SWE values from noisy data with an average error of 11.0%. This compares favorably with the measured accuracy of physical field sampling techniques currently used by water resource managers. More work is needed to validate our results with field data, but we conclude that GPR has the potential to recover SWE accurately in stratified and homogeneous snow under both wet and dry conditions with semi-automated processing techniques.

REFERENCES CITED

[1] T P Barnett, J C Adam, and D P Lettenmaier. Potential impacts of a warming climate on water availability in snow-dominated regions. *Nature*, 438(7066):303–309, 2005. doi: 10.1038/nature04141.

[2] Dongyue Li, Melissa L. Wrzesien, Michael Durand, Jennifer Adam, and Dennis P. Lettenmaier. How much runoff originates as snow in the western United States, and how will that change in the future? *Geophysical Research Letters*, 44:6163–6172, 2017. doi: 10.1002/2017GL073551.

[3] Colorado historical snowpack percentage time series charts. https://www.nrcs.usda.gov/wps/portal/nrcs/detail/co/snow/products/, 2020. Accessed: 2020-11-10.

[4] Automated snow monitoring. nrcs.usda.gov/wps/portal/wcc/home/aboutUs/monitoringPrograms/automatedSnowMonitoring/, 2021. Accessed: 2020-03-30.

[5] Noah P. Molotch and Roger C. Bales. Scaling snow observations from the point to the grid element: Implications for observation network design. *Water Resources Research*, 41(11):1–16, 2005. ISSN 00431397. doi: 10.1029/2005WR004229.

[6] Debbie Clifford. Global estimates of snow water equivalent from passive microwave instruments: history, challenges and future developments. *International Journal of Remote Sensing*, 31(14):3707–3726, 2010. doi: 10.1080/01431161.2010.483482.

[7] Thomas H. Painter, Daniel F. Berisford, Joseph W. Boardman, Kathryn J. Bormann, Jeffrey S. Deems, Frank Gehrke, Andrew Hedrick, Michael Joyce, Ross Laidlaw, Danny Marks, Chris Mattmann, Bruce McGurk, Paul Ramirez, Megan Richardson, S. McKenzie Skiles, Felix C. Seidel, and Adam Winstral. The airborne snow observatory: Fusion of scanning lidar, imaging spectrometer, and physically-based modeling for mapping snow water equivalent and snow albedo. *Remote Sensing of Environment*, 184:139 – 152, 2016. ISSN 0034-4257. doi: https://doi.org/10.1016/j.rse.2016.06.018.

[8] A. P. Annan. *11. Ground-Penetrating Radar*, chapter 11, pages 357–438. Society of Exploration Geophysicists, 2012. doi: 10.1190/1.9781560801719.ch11.

[9] Martti E. Tiuri, Ari H. Sihvola, Ebbe G. Nyfors, and Martti T. Hallikaiken. The Complex Dielectric Constant of Snow at Microwave Frequencies. *IEEE Journal of Oceanic Engineering*, 9(5):377–382, 1984. ISSN 15581691. doi: 10.1109/JOE.1984.1145645.

[10] D A Ellerbruch and H S Boyne. Snow stratigraphy and water equivalence measured with an active microwave system. *Journal of Glaciology*, 26(94), 1980. doi: https://doi.org/10.3189/S0022143000010765.

[11] H Gubler and M Hiller. The use of microwave fmcw radar in snow and avalanche research. *Cold regions science and technology*, 9(2):109–119, 1984. ISSN 0165-232X.

[12] Knut Sand and Oddbjørn Bruland. Application of georadar for snow cover surveying: Paper presented at the 11th northern res. basins symposium/workshop prudhoe bay to fairbanks, alaska, usa–aug. 18-22, 1997. *Hydrology Research*, 29(4-5):361–370, 1998.

[13] Joel T. Harper and John H. Bradford. Snow stratigraphy over a uniform depositional surface: Spatial variability and measurement tools. *Cold Regions Science and Technology*, 37(3):289–298, 2003. ISSN 0165232X. doi: 10.1016/S0165-232X(03)00071-5.

[14] Wolf-Dietrich Marchand, Ånund Killingtveit, Peter Wilén, and Per Wikström. Comparison of Ground-Based and Airborne Snow Depth Measurements with Georadar Systems, Case Study: Paper presented at the Nordic Hydrological Conference (Røros, Norway 4-7 August 2002). *Hydrology Research*, 34(5):427–448, 10 2003. ISSN 0029-1277. doi: 10.2166/nh.2003.0016.

[15] Hans-peter Marshall, Gary Koh, and Richard R Forster. Estimating alpine snowpack properties using FMCW radar. *Annals of Glaciology*, 40:157–162, 2005. doi: 10.3189/172756405781813500.

[16] Hans-Peter Marshall and Gary Koh. Fmcw radars for snow research. *Cold Regions Science and Technology*, 52(2):118 – 131, 2008. ISSN 0165-232X. doi: https://doi.org/10.1016/j.coldregions.2007.04.008. Research in Cryospheric Science and Engineering.

[17] Angela Lundberg, Nils Granlund, and David Gustafsson. Towards automated 'ground truth' snow measurements—a review of operational and new measurement methods for sweden, norway, and finland. *Hydrological Processes*, 24(14):1955–1970, 2010. doi: https://doi.org/10.1002/hyp.7658.

[18] James St Clair and W. Steven Holbrook. Measuring snow water equivalent from common-offset GPR records through migration velocity analysis. *Cryosphere*, 11(6): 2997–3009, 2017. ISSN 19940424. doi: 10.5194/tc-11-2997-2017.

[19] Ryan W Webb. Using ground penetrating radar to assess the variability of snow water equivalent and melt in a mixed canopy forest, northern colorado. *Frontiers of Earth Science*, 11(3):482–495, 2017. doi: 10.1007/s11707-017-0645-0.

[20] Daniel McGrath, Louis Sass, Shad O'Neel, Chris McNeill, Salvatore G Candela, Emily H Baker, and Hans-Peter Marshall. Interannual snow accumulation variability on glaciers derived from repeat, spatially extensive ground-penetrating radar surveys. *The Cryosphere*, 12:3617–3633, 2018. doi: 10.5194/tc-12-3617-2018.

[21] Daniel McGrath, Ryan Webb, David Shean, Randall Bonnell, Hans-Peter Marshall, Thomas H. Painter, Noah P. Molotch, Kelly Elder, Christopher Hiemstra, and Ludovic Brucker. Spatially extensive ground-penetrating radar snow depth observations during nasa's 2017 snowex campaign: Comparison with in situ, airborne, and satellite observations. *Water Resources Research*, 55(11):10026–10036, 2019. doi: https://doi.org/10.1029/2019WR024907.

[22] Christoph Mitterer, Achim Heilig, Jürg Schweizer, and Olaf Eisen. Upward-looking ground-penetrating radar for measuring wet-snow properties. *Cold Regions Science and Technology*, 69(2):129 – 138, 2011. ISSN 0165-232X. doi: https://doi.org/10.1016/j.coldregions.2011.06.003. International Snow Science Workshop 2010 Lake Tahoe.

[23] A. Heilig, C. Mitterer, L. Schmid, N. Wever, J. Schweizer, H.-P. Marshall, and O. Eisen. Seasonal and diurnal cycles of liquid water in snow—measurements and modeling. *Journal of Geophysical Research: Earth Surface*, 120(10):2139–2154, 2015. doi: https://doi.org/10.1002/2015JF003593.

[24] John H. Bradford, Joel T. Harper, and Joel Brown. Complex dielectric permittivity measurements from ground-penetrating radar data to estimate snow liquid water content in the pendular regime. *Water Resources Research*, 45(8), 2009. ISSN 00431397. doi: 10.1029/2008WR007341.

[25] Tim Bergmann, Johan A Robertsson, and Klaus Holliger. Finite-difference modeling of electromagnetic wave propagation in dispersive and attenuating media. *Geophysics*, 63 (3):856–867, 1998. doi: 10.1190/1.1444396.

[26] G E Archie. The Electrical Resistivity Log as an Aid in Determining Some Reservoir Characteristics. *Transactions of the AIME*, 146(01):54–62, dec 1942. ISSN 0081-1696. doi: 10.2118/942054-G.

[27] Russell P Wharton, Gary A Hazen, Rama N Rau, David L Best, et al. Advancements in electromagnetic propagation logging. In *SPE Rocky Mountain Regional Meeting*. Society of Petroleum Engineers, 1980.

[28] J. B. Hasted. *Aqueous Dielectrics*. Chapman and Hall, 1973.

[29] Sergey Fomel, Evgeny Landa, and M Turhan Taner. Poststack velocity analysis by separation and imaging of seismic diffractions. *Geophysics*, 72(6):6–11, 2007. doi: 10.1190/1.2781533.

[30] R H Stolt. Migration by fourier transform. *Geophysics*, 43:23–48, 1978. doi: 10.1190/1.1440826.

[31] C. Hewitt Dix. Seismic velocities from surface measurements. *Geophysics*, 20(1):68–86, 1955. ISSN 0016-8033.

[32] John H Bradford. Frequency-dependent attenuation analysis of ground-penetrating radar data. *Geophysics*, 72(3):J7–J16, 2007. doi: 10.1190/1.00V7215.

[33] Greg Turner. Subsurface radar propagation deconvolution. *Geophysics*, 59(2):215–223, 1994. doi: 10.1190/1.1443583.

[34] Greg Turner and Anthony F Siggins. Constant Q attenuation of subsurface radar pulses. *Geophysics*, 59(8):1192–1200, 1994. doi: 10.1190/1.1443677.

[35] John H. Bradford, David F. Dickins, and Per Johan Brandvik. Assessing the potential to detect oil spills in and under snow using airborne ground-penetrating radar. *GEOPHYSICS*, 75(2):G1–G12, 2010. doi: 10.1190/1.3312184.

[36] David J Griffiths. *Introduction to Electrodynamics; 4th ed.* Pearson, Boston, MA, 2013. doi: 1108420419.

[37] J. M Carcione, G Lenzi, and S Valle. Gpr modelling by the fourier method: improvement of the algorithm. *Geophysical Prospecting*, 47(6):1015–1029, 1999. ISSN 0016-8025. doi: 10.1046/j.1365-2478.1999.00151.x.

[38] James D Irving and Rosemary Knight. Removal of wavelet dispersion from ground-penetrating radar data. *Geophysics*, 68(3):960–970, 2003. doi: 10.1190/1.1581068.

[39] David Dixon and Sarah Boon. Comparison of the snowhydro snow sampler with existing snow tube designs. *Hydrological Processes*, 26(17):2555–2562, 2012. doi: https://doi.org/10.1002/hyp.9317.

[40] Mala drone gpr. https://www.malagpr.com.au/geo$_g pr_d rone.html$, 2021. $Accessed$: $2021 - 11 - 5$.

[41] Ugcs airborne gpr solution. https://integrated.ugcs.com/gpr, 2021. Accessed: 2021-11-5.

[42] Geoscanners ab spg-1700. https://geo-matching.com/gpr-ground-penetrating-radars/spg-1700, 2021. Accessed: 2021-11-5.

APPENDIX
COPYRIGHT PERMISSIONS

SEG follows STM permissions guidelines, to which many publishers of scholarly works are signatories. Under this framework, it is not necessary for authors, editors, or publishers to obtain explicit written permission from SEG to republish the following amounts of content from Society publications with respect to a particular journal article, conference paper, book, or derivative work being prepared for publication and/or distribution:

1. up to three figures (including tables) from a journal article or book chapter, but:

   (a) not more than five figures from a whole book or journal issue/edition;

   (b) not more than six figures from an annual journal volume;

   (c) and not more than three figures from an SEG article, and not more than three figures from works published in an SEG book chapter (and in total not more than thirty SEG figures for republication in a book, including a multivolume book, with different authors per chapter)

2. single text extracts of fewer than 400 words from a journal article or book chapter, but not more than a total of 800 words from a whole book or journal issue/edition.

There are no fees associated with permission grants for republication of SEG material in quantities consistent with the guidelines above. Authors or instructors who need documentation that SEG is extending this permission are encouraged to print this message. Those who require further documentation should contact the SEG publications director.

SEG requires that full acknowledgment of the source, including a DOI-based permalink (live in electronic versions), be used in any new work that includes SEG material. If SEG has cited a publication for which it is not the publisher, and a third party seeks permission to republish material from that publication, permission should be obtained from the original publisher.

Source: library.seg.org/page/policies/permissions